



1 8 0 3

UNIVERSITY OF ANTIOQUIA

Mass Modelling gfdgfdgdf of Globular Cluster ω Centauri

by

Juan Manuel Espejo Salcedo

Advisor:

Juan Carlos Muñoz Cuartas

A thesis submitted in partial fulfillment for the
degree of Astronomer

in the
Natural Sciences Faculty
Institute of Physics

April 2016

*“We are just an advanced breed of monkeys on a minor planet of a very average star.
But we can understand the Universe. That makes us something very special.”*

Stephen Hawking

Abstract

Natural Sciences Faculty
Institute of Physics

The study of the dynamics and mass modelling of galaxies is a very complex but beautiful branch of modern Astrophysics and Cosmology. When you follow this route it is perhaps inevitable the need of studying stellar systems inside galaxies because they are inherent all along the way of the history and the formation and structure of galaxies themselves. This thesis work is intended to show our work on mass models of Globular Clusters in the Milky Way with our own data obtained in OPD observatory. By using spectra of the central region of the clusters we compute radial velocities of the stars to obtain information about the velocity dispersion profile thus obtaining information about the potential well responsible for the dynamics of those individual stars. With this information, aside the mass estimations given by the photometry results we can build mass models of the clusters looking for insight on the amount of dark matter present in this kind of structures, if dark matter is present at all.

Acknowledgements

The acknowledgements and the people to thank go here, don't forget to include your project advisor...

Contents

| | |
|---|------|
| Abstract | ii |
| Acknowledgements | iii |
| List of Figures | vi |
| List of Tables | viii |
| 1 Introduction | 1 |
| 2 Theoretical Framework | 4 |
| 2.1 Basics | 4 |
| 2.2 Formation and evolution | 7 |
| 2.3 Observational Properties | 11 |
| 2.4 ω Centauri | 17 |
| 2.5 Mass models and Dynamics | 17 |
| 2.5.1 Potential Theory of Spherical Systems | 17 |
| 2.5.2 Collisionless Systems | 23 |
| 2.5.3 Dynamics | 24 |
| 3 Observations and Analysis | 30 |
| 3.1 Observational Procedures | 30 |
| 3.1.1 Spectroscopic Data | 31 |
| 3.1.2 Photometric Data | 34 |
| 3.2 First step for Anaysis | 35 |
| 3.3 Photometry | 36 |
| 3.3.1 Aperture Photometry | 38 |
| 3.3.2 PSF Photometry | 41 |
| 3.4 Spectroscopy | 44 |
| 3.4.1 Spectroscopic Reduction | 44 |
| 3.4.2 Extraction | 46 |
| 3.4.3 Wavelength Calibration | 47 |
| 3.4.4 Flux Calibration | 50 |
| 3.5 Radial velocity determination | 53 |
| 3.5.1 RVSAO | 54 |

| | |
|---|-----------|
| 3.5.2 FXCOR | 57 |
| 3.6 Databases | 59 |
| 4 Modelling | 61 |
| 4.1 Modified Hernquist Model | 61 |
| 4.1.1 Full Modelling | 66 |
| 4.1.2 Fix mass-to-light ratio | 68 |
| 4.2 Stellar Population Synthesis with Starlight | 71 |
| 5 Conclusions | 78 |
| Bibliography | 79 |

List of Figures

| | | |
|------|--|----|
| 2.1 | M15 Globular cluster | 5 |
| 2.2 | ESO and Hubble images of Globular Clusters | 6 |
| 2.3 | Evolution of an ergodic Plummer model over time | 10 |
| 2.4 | Evolution of the velocity anisotropy parameter | 11 |
| 2.5 | Hubble image of Fornax-2 Globular Cluster | 13 |
| 2.6 | Hubble Space Telescope image of Fornax-3 Globular Cluster | 13 |
| 2.7 | Color Magnitude diagram of M55 | 15 |
| 2.8 | HR Diagram for Stars | 15 |
| 2.9 | Illustration of the orbits of Globular Clusters around a spiral galaxy | 16 |
| 3.1 | OPD Observatory | 31 |
| 3.2 | Perkin-Elmer telescope used for Spectroscopy | 31 |
| 3.3 | IAG Telescope used for Photometry | 34 |
| 3.4 | Dirty image of NGC5139 | 37 |
| 3.5 | Clean image of NGC5139 | 37 |
| 3.6 | Normalized Superflat for the filter I | 38 |
| 3.7 | NGC5139 as observed in the V filter | 39 |
| 3.8 | Photometry results of Magnitudes vs Size of apertures | 40 |
| 3.9 | PSF modelling | 42 |
| 3.10 | PSF residuals | 42 |
| 3.11 | PSF image created by the task Seepsf | 43 |
| 3.12 | Pf | 44 |
| 3.13 | Dirty spectrum of NGC5139 | 46 |
| 3.14 | Clean spectrum of NGC5139 | 46 |
| 3.15 | Spectrum of calibration star HR4468 | 47 |
| 3.16 | Emission lines for the Ne-Ar calibration lamp | 48 |
| 3.17 | Theoric emisison lines of a Ne-Ar lamp | 48 |
| 3.18 | Wavelength calibrated spectrum of HR4468 | 49 |
| 3.19 | Comparison between the two wavelength calibration methods | 50 |
| 3.20 | Zoomed comparison between the two wavelength calibration methods | 50 |
| 3.21 | Flux calibrated spectrum of HR4468 | 52 |
| 3.22 | Spectrum of a prominent star of the NGC5139 globular cluster | 53 |
| 3.23 | XCSAO results | 54 |
| 3.24 | Results of the template spectrum created by rspectext | 55 |
| 3.25 | The nature of the barycenter shift of radial velocities | 56 |
| 3.26 | EMSAO results with the identification of lines | 57 |
| 3.27 | FXCOR results for NGC1904 | 58 |

| | |
|---|----|
| 4.1 Pg | 64 |
| 4.2 Pg | 65 |
| 4.3 Pg | 67 |
| 4.4 Pg | 68 |
| 4.5 Pg | 69 |
| 4.6 Pg | 70 |
| 4.7 Pg | 71 |
| 4.8 Extinction Correction | 73 |
| 4.9 Synthetic spectrum of STARLIGHT | 73 |
| 4.10 En | 75 |
| 4.11 En | 76 |
| 4.12 En | 76 |
| 4.13 En | 77 |

List of Tables

| | | |
|-----|--|----|
| 2.1 | Two power density potentials | 21 |
| 3.1 | Observed objects in OPD | 33 |
| 3.2 | Input data for the creation of template with rspecText | 55 |
| 3.3 | Database | 59 |
| 3.4 | Mass Omega Centauri | 60 |
| 4.1 | It | 67 |
| 4.2 | It | 68 |
| 4.3 | It | 70 |
| 4.4 | It | 71 |
| 4.5 | Mass Omega Centauri | 75 |
| 4.6 | It | 75 |
| 4.7 | It | 76 |
| 4.8 | It | 77 |
| 4.9 | It | 77 |

For/Dedicated to/To my...

Chapter 1

Introduction

Old Globular Clusters are among of the oldest known subunits of galaxies, so that they might hold the key of understanding the galaxies' very first evolution stages and their formation. In particular, the amount of dark matter that they could (or not) have could provide valuable information to the current theories about the creation and early development of the Milky Way (and other galaxies in general). Even though there is a large amount of observational data that has been obtained since the late 18th century, and many advances in theoretical work involving their photometric properties, trajectories and star formation, there is not yet an accepted model to describe the early formation of these ancient structures nor a clear understanding of their mass content. In addition, recent observations show that their stellar populations are far more complex than initially thought (R. G. Gratton et. al. 2012 [8]), an issue that is directly connected to the formation process itself.

In order to access the problem of their formation, many theories have been considered, although there are two that stand out the most: One states that Globular Clusters were the very first condensed systems to form in the early universe, by the time big structures such as galaxies were only about to start their formation. The second possibility is that they originated in larger star-forming systems that later merged to form the present galaxies. These two broad possibilities are discussed in detail by Larson (1996) [9].

The first possibility (suggested by Peebles & Dicke in 1968 [7]) says that Globular Clusters (GCs) were formed by a process of Jeans instability in the early universe, they suggest that the smallest gravitationally unstable clouds that were produced right after the recombination from isothermal perturbations were the progenitors of GCs, this possibility is in concordance with the current scenario of galaxy formation in which galaxies are formed inside the deepest regions of the gravitational potential well provided by dark matter halos and it has been received with great interest by the scientific community

since it not only fits within the hierarchical scenario of structure and galaxy formation, but also may help to understand some of the open problems such as the missing satellites around galaxies like ours (Klypin et. al. 1999) [11]. However, evidence has been found against this scenario. One is the fact that this early attempt did not take into account the issues of the multiple stellar generations that have been recently found in these stellar systems. Another problem is the findings of tidal tails surrounding GCs, which is not expected if these structures are formed and reside inside their own extended dark matter halos (Odenkirchen et al. (2003))[12].

Regarding the second possibility, Fall & Rees (1985, 1988)[13] proposed that the formation of globular clusters was the product of the collapsing gas of a protogalaxy. The mechanism would be the response to thermal instabilities in the hot gaseous halos of massive galaxies, this hypothesis starts from the assumption that star formation can only occur when the gas has been able to cool in a free-fall time. The Fall & Rees hypothesis has been popular among theorists who have used it to predict the characteristic properties of globular clusters such as its poor gas content, although it has proven difficulties to justify the assumed thermal behaviour of the cluster-forming gas clouds in many regions of the galaxy. This scenario presents other problems since there are observations such as those made by Sharina et. al. 2005 [10] that suggest that very low mass galaxies, not massive enough to host a hot gaseous halo, may also have their own GCs , so that their formation might be the result of a different mechanism.

Not only the formation of these structures is puzzling, their composition is also a challenging problem because some authors argue that these structures do not contain any dark matter contributions and that their dynamics can be explained completely with the baryonic matter inside them. For example, Conroy et. al. (2011) [14] used density profiles to argue against the presence of dark matter inside globular clusters by demonstrating that the outer stellar density profile of isolated GCs is very sensitive to the presence of an extended dark halo which is not seen in the observations of NGC 2419; while Ibata et. al. (2013) [5] have found that under general conditions it could be possible to find significant fractions of dark matter in globular clusters, by using a Markov-Chain Monte Carlo approach and modelling current observations. Modelling the mass content of GCs in the galaxy would help to disentangle the mechanism driving its formation process and would give us some insight into their stellar populations as well. Detailed mass modelling would allow us to study the mass distribution in the inner region of globular clusters, giving us information about the dominant components, just like Adams J. J. et. al., 2012 did with NGC2976 [6]. Providing light on the problem of the origin of globular clusters.

Our aim in this thesis is to build our own mass model for Globular Clusters using multiple spectroscopic and photometric observations of ω Centauri so that we can be able to discuss and find new evidence on the existence or absence of dark matter in them according to these results.

With our set of data, and the back up of Cerro Tololo observations for comparison, we do the preliminary reduction and analysis of photometric and spectroscopic data, including the wavelength and flux calibration of the spectra. The photometric data will show us the mass to light ratio of the Globular Clusters thus giving us information about the baryonic mass content of the clusters. On the other hand, the spectroscopic data will give us information about the radial velocity of the stars that will provide us the statistical dispersion of velocities in the inner region of the clusters thus giving us information about the potential well in the clusters. This procedure is done using the Radial Velocity Package of IRAF called *RVSAO* which uses cross correlation techniques in the Fourier transform of templates and scientific spectra to infer the doppler broadening of the emission and/or absorption lines in our data and allows us to calculate their radial velocities. The spectroscopic data will also give us information about the stellar populations of the clusters so that we can also infer the baryonic mass using this technique.

The bulk properties of GCs, with the possible exception of their innermost regions, can be modelled using the collisionless Boltzmann equation (Binney & Tremaine 1987) [3], from which the statistical properties of the velocity distribution of stars can be derived. In particular, one can derive a formulation for the velocity dispersion tensor that, in the isotropic, non rotating case, reduces to a scalar quantity (as discussed in further detail in the next chapter). This quantity can be determined using the appropriate Jeans equations. Most of these calculations require knowledge of the distribution function (DF) that determines the number of stars in a given region of space, and the gravitational potential.

The best fit for our data with the theoretical assumptions will tell us how mass is distributed in the clusters and it will allow us to conclude if there is a significant contribution of dark matter to the potential well that provides the stars the observed velocities. As mentioned before, the Mass Modelling will let us have a good insight into the problem of the formation of these structures.

Chapter 2

Theoretical Framework

Typical galaxies all around the Universe hold different structures such as stellar systems of between 10^2 and 10^6 stars which orbit their galactic core . We call these interesting systems star clusters and they are basically divided into three main types: Open Clusters, stellar associations and **Globular Clusters**. Open clusters are stellar systems that can contain from hundreds to thousands of stars, they are formed continuously in the Galactic disk and most of them are relatively young (younger than 1 Gyr). Old open clusters are rare since their gravitational stability is very low and can be easily disrupted by gravitational shocks from passing interstellar gas clouds. It seems likely that most of the stars in the galactic disk were formed in open clusters that have dissolved since then.

Stellar associations such as young associations of stars that can contain 10 to 100 massive stars of spectral class O and B, and are known as OB associations. These associations also contain hundreds or thousands of low- and intermediate-mass stars.

Globular clusters, the other important class of stellar systems, are much more interesting and we focus deeply on their properties and characteristics.

2.1 Basics

Globular clusters are very massive, bound stellar systems that can contain from thousands to millions of stars in a nearly spherical distribution spread over a volume of tens of parsecs in diameter. These stellar systems are composed of old stars and they do not contain a significant amount of gas or dust. As an example, figure 2.1 shows M15 Globular Cluster, discovered by Jean-Dominique Maraldi in 1746 while he was studying the De Chseaux comet, the cluster shows the spherical symmetry and a higher stellar

density in the center, it can also be seen that most of the cluster brightness is given by the stars and not by dust or gas.



FIGURE 2.1: Globular Cluster M15, taken by the Hubble Space Telescope with an exposition time of 900 seconds. The spherical symmetry that is clearly seen is one of GCs' most representative properties. Image by NASA

These stellar structures are compact, gravitationally bound groups of hundreds of thousands to several million stars that are themselves gravitationally bound to galaxies. They have comparable ages to their associated galaxies which is an encouraging characteristic to study them as they could provide valuable information about the formation and evolution of their host galaxies.

Their star populations are uniformly old, although different stellar populations are found as we improve our measurements and observations, such as in the case of the recent study of the stellar populations in the globular clusters of the Fornax dwarf galaxy, where multiple stellar populations and nitrogen abundances have been found (Larsen & Brodie et al. 2014) [15]. Globular clusters are devoid of gas so that pretty much no new stars form in them. The stars at the centre of a globular cluster are much more densely packed than the stars in other parts of the galaxy, providing a rather hostile scenario for the formation of habitable planets.

Globular clusters revolve about the nucleus of a galaxy on orbits of high eccentricity and high inclination to the galactic plane. About a third of globular clusters are concentrated

around the galactic center. A typical cluster has a period of revolution around the order of 10^8 years. A cluster spends most of its time far from the center of a galaxy, and so most of them can, and have been discovered in the spaces between galaxies.

Due to clusters moving in various orbits in the Galaxy, they are bound together with gravitational forces that are stronger than the disrupting forces exerted on it by the Galaxy or other nearby stars, and this results in an added condition for the stability of a cluster.

The spherical shape of these systems is due to the stability that they can acquire over time. To ensure the stability of an isolated cluster, the average speed of its individual stars must not exceed the escape velocity from the cluster. If this occurred, the stars would escape into space, and the cluster would dissipate. If the stellar velocities are low enough to satisfy this condition, then the cluster is gravitationally bound, i.e. the force of gravity is strong enough to keep the member stars from escaping.

Another factor in the stability of clusters is size; the smaller and more compact the cluster, the greater its own gravitational binding force compared with the disrupting forces, and the more chance it has to survive to old ages.

Because globular clusters are highly compact systems, they are consequently very stable, and so most globular clusters will probably maintain their identity almost all of their lifetimes. But even these clusters lose some stars, especially if they have a low mass. This is because there are always some stars in the cluster that can eventually reach velocities high enough for them to leave the gravitational pull provided by the mass of the cluster.

When a star escapes, it carries with it energy, removing this energy from the cluster as a whole. This eventually results in the cluster developing a tightly bound core surrounded by a rarefied halo of stars as we can see in the following images of Globular Clusters:



FIGURE 2.2: Globular Clusters taken by ESO and the HST. From left to right: M4 (ESO), Omega Cen (ESO) and M80 (Hubble). Images from the Hubble Space Telescope database.

In the dense core of a cluster, the stars occasionally collide, and some of the debris eventually coalesces. Predictions indicate that this dynamical evolution could lead to the development of a large Black Hole at the cluster's center. At the same time, a few stars in the outer parts of the cluster would continue to escape. The escape rate and dynamical evolution for the rich globular clusters are so slow that the clusters can easily survive for many billions of years, remaining mostly unchanged.

Observations and mass models of these structures show that the average star density in a Globular Cluster is about 0.4 stars per cubic parsec. In the dense center of the cluster, the star density can increase from 100 to 1000 stars per cubic parsec. However, even in the center of clusters, there is still plenty of space between the stars.

In order to understand how dense Globular Clusters can be, we may think of a clear example like Proxima Centauri, which is about 1.3 parsecs from Earth. Thus, if we were able to draw a sphere around the Sun with a radius of 1.3 parsecs, it would only contain 2 stars: the Sun and Proxima Centauri. But if you were to draw this same sphere in the center of the globular cluster M13, it would contain approximately 10,000 stars.

2.2 Formation and evolution

The formation of Globular Clusters is not well understood yet, and we only have crude ideas of their typical states right after they have reached the dynamical equilibrium. As it was mentioned in the introduction, two main broad types of possibilities have been considered to explain the very first processes that created these structures.

The first scenario suggests that in the early universe the first structures that came to exist were globular clusters formed by Jeans instability. One of the main contributions to this possibility was given by Peebles & Dicke (1968) [7] who first pointed out that globular clusters might have formed even before the collapse of the protogalaxy, noting the fact that the baryonic Jeans mass right after decoupling is about the size of a Globular Cluster. Although their possibility is in concordance with the current scenario of galaxy formation, there are still problems of this theory, for example, it cannot explain why there are so few intergalactic globular clusters and why the properties of globular clusters are correlated with their host galaxies. As mentioned before, another problem with this theory are the observational results of Odenkirchen et al. (2003) [12] of the tidal tails of some GCs that could not exist if these stellar systems had their own dark matter halos that would keep the stability and thus avoiding the creation of these tidal tails.

The second formation scenario suggests that Globular Clusters are secondary objects, and they could have been formed by thermal instabilities in cooling halo gas or by gravitational instabilities in giant bubbles or even by the shocked layers between two colliding clouds.

The theory about the thermal instabilities in cooling halo gas proposed by Fall & Rees (1985, 1988)[13] suggests that cold dense clouds condense out of hot and tenuous background to form as progenitors of globular clusters. This idea could be in accordance with the present observational properties of Globular Clusters like their characteristic metallicity. Yet again, this theory has proven difficulties to justify the assumed thermal behaviour of the cluster-forming gas clouds and the existence of globular clusters in very low mass galaxies.

The idea that GCs were formed by gravitational instabilities in giant bubbles and busted by the shock of layers between two or more colliding clouds has been defended by some authors such as Murray & Lin (1992) who have argued that self-gravitating clouds are unstable to fragmentations and spontaneous star formation so that these stellar systems must form from sub-Jeans mass clouds. In subsequent work, published in 1993 by Murray et al., it has been shown that only clouds in a limited mass range ($10^4 M_\odot \lesssim M \lesssim 10^6 M_\odot$) can survive both the Kelvin-Helmholtz instability of the gas and the thermal instability of the system which does not lead to bound clusters. Clouds within this critical mass range will form globular clusters if they are induced into cooling and collapse by collisions with sufficient velocity. As it can be seen, the formation of these ancient structures is in a current debate and is directly correlated with the formation of galaxies itself so they could provide answer to our ever changing modelling.

Moving on to the evolution of these systems, we note that our current observations and modelling give us good results after the equilibrium has been reached, in this context, there must be mentioned that the mechanism that drives the system to stability is **relaxation** (explained in the next section). This process pretty much erases the cluster's memory of its initial state so the results for gravitational stable systems can be reached using a wide range of initial conditions and they can be easily modelled.

For a typical Globular Cluster with $N = 10^5$ stars and a radius of $r = 10\text{pc}$ the relaxation time would be around $t_{\text{relax}} = 10^9 \text{ years}$ which is much smaller than the age of the stars in the GC so that stability can (and is observed to) be easily reached. Since the relaxation time is inversely proportional to density, then evolution due to this mechanism proceeds most rapidly in the dense central regions of the clusters. Within this central region that is relaxed, the distribution function f and the density distribution should be approximate to a isothermal distribution, this means that the distribution function must be approximately Maxwellian at energies well below the escape energy. We assume

that in the outer parts of the clusters the relaxation time is long and encounters have relatively little effect.

Other important characteristic of their evolution is that they lose mass from stellar evolution: Our stellar evolution theories show us that stars usually eject mass from their surfaces near the ends of their lives, this is a well studied problem. For the mass-losing stars inside globular clusters, the ejected mass is likely to escape the cluster, either because the ejection velocity exceeds the escape speed from the cluster or because it interacts with the galactic gas when the cluster is passing through the disk, assuming this is the case. So we can conclude that the clusters lose mass as stars evolve. It must be mentioned that the evolution time scale of a typical population of stars is usually much longer than the crossing time in the cluster.

The mass lost by a cluster due to stellar evolution depends on the initial mass function which specifies the distribution of masses of stars just after they have formed and the initial-final mass function.

Now, when we talk about the evolution of Globular Clusters, we must see how the mass distribution evolves over time mainly because this will help us to better understand their formation. The evolution of the mass distribution in an isolated cluster such as a GC that is far enough from the disk to have few important encounters and collisions, can be modelled using the simple but powerful Plummer model that we shall introduce in the following section as shown in the next figure:



FIGURE 2.3: Evolution of an ergodic Plummer model over time, according to an orbit-averaged Monte-Carlo solution of the Fokker Planck equation with 3×10^5 superstars (heavy solid lines) and an N-body simulation with 65536 superstars (dots, connected by solid lines).

From Freigat, Rasio, & Baumgardt (2006)

As we can see above, the outer half of the cluster expands, mainly due to the gradual growth of the halo as stars in the core diffuse towards the escape energy, but the most important feature of this figure, is that we can see that the center contracts or gets smaller, this process is known as **core collapse** and it leads to a dramatic growth in the central density that may indicate the existence of an apparent singularity in the central density such as a black hole.

Takahashi, 1995 found a more accurate calculation of core collapse in a spherical cluster (without binaries) starting from a Plummer model. His calculations allow greater dynamic range than Monte Carlo or N-body methods. His results show that as the cluster evolves, the core radius shrinks and the central density grows, as seen in the above figure. Outside the core, the density profile approaches a power law of the form $\rho \propto r^{-2.23}$.

Another interesting result regarding Takahashi's method based on the direct solutions of the orbit-averaged Fokker Planck equations (partial differential equations that describe the time evolution of the probability density function of the velocity of a particle under

the influence of dragging and random forces) is the behaviour of the anisotropy parameter $\beta = 1 - \bar{v}_\theta^2/\bar{v}_r^2$ as we can see in the following figure:

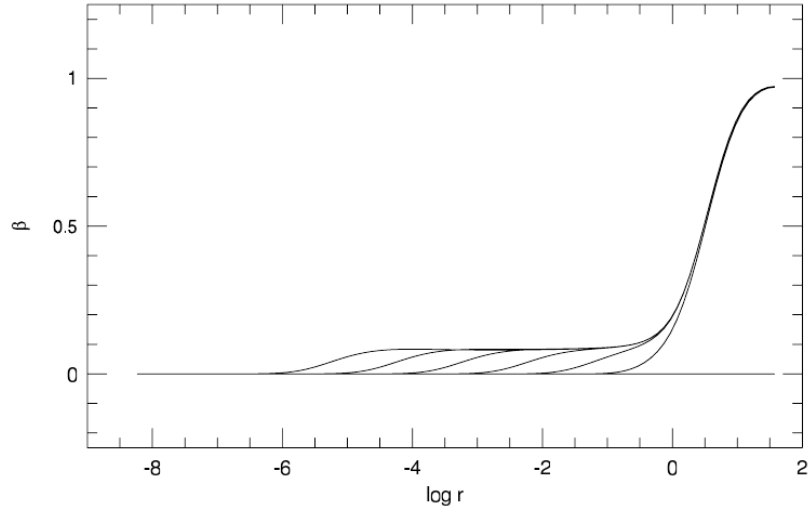


FIGURE 2.4: The evolution of the velocity anisotropy parameter for an orbit-averaged Fokker Planck calculation of core collapse. From Takahashi (1995)

At large radii, the anisotropy parameter (that indicates the tendency of the system to have or not preferred directions) tends to unity ($\beta \simeq 1$), and that indicates that the orbits are nearly radial, at the smallest radii, inside the shrinking core, we have $\beta \simeq 0$, which indicates that the velocity distribution is isotropic. We note that in the radius range in which the density profile in the top panel is a power law, there is a constant small radial anisotropy of $\beta \simeq 0.08$ or $\bar{v}_\theta^2/\bar{v}_r^2 \simeq 0.92$. We will discuss the details of these parameters in the next section.

Now, regarding the late interactions and accretion processes that could affect the evolution of GCs, we note that although our Galaxy has evidently not experienced any further major accretion events capable of disrupting the disk, it is possible that minor accretion events affecting only the halo and not the disk have continued to occur as suggested by Navarro, Frenk, & White 1994, but their net effect on the GC's dynamics and stability in the context of cosmology is very low.

The evolution process for these systems is so long that it fits entirely in the context of Cosmology. Most of the clusters whose masses are larger than $10^5 M_\odot$ have lifetimes longer than the Hubble time.

2.3 Observational Properties

Scenario and Observations

Galactic Globular Clusters are relatively easy to observe because they are close to us in the galactic context and their big size makes them bright objects, for this reason, they have been observed even since the 17th century. The first globular cluster discovered, but then taken for a nebula, was M22 in Sagittarius, which was probably discovered by Abraham Ihle in 1665. This discovery was followed by that of southern ω Centauri (NGC5139) by Edmond Halley in 1677, which is the largest known globular cluster in our galaxy and also a former galactic-nucleus candidate. This “nebula” had been known but classified as star since ancient times. The next discovery was made by Gottfried Kirch in 1702 M5 in Serpens Caput, and then M13 in Hercules, again by Halley, in 1714. Charles Messier was the first to resolve one globular cluster, M4, but still referred to the other 28 of these objects in his catalog as “round nebulae”.

Currently, there are about 150 confirmed Globular Clusters in the Milky Way and the number is growing since we are improving our techniques to find globular clusters that may be passing through the disk and thus are difficult to observe.

One important development in recent years is some debated observational evidence that dense, massive star clusters are currently forming in certain environments. It has been suggested that these objects are young globular clusters. This idea is not universally accepted, both because current observations are not definitive and possibly because of the notion of globular clusters as ancient objects. However, if globular clusters are forming at the present epoch, we will have the opportunity to study the formation process directly. It seems inevitable that this will greatly enhance our understanding of how and why globular clusters form, as well as deepening our knowledge of the galaxy formation process to which globular cluster formation is intimately related.

Some other observational results of GCs in other galaxies just broadens the current scenario of formation and evolution, for example, in November, 2014 Tim Stephens from the University of California studied images taken by the HST of four globular clusters located in the small galaxy Fornax to study their properties and compare them with GCs in the Milky Way. What these observations show is that the GCs in the dwarf galaxy Fornax are very similar to our GCs and so they must have formed in a similar way, however, these findings don’t fit with the leading theories that have been developed to explain how globular clusters form.



FIGURE 2.5: Image of Fornax-2 Globular Cluster taken by the Hubble Space Telescope. From University of California newscenter.



FIGURE 2.6: Hubble Space Telescope image of Fornax-2 Globular Cluster. From University of California newscenter.

As mentioned before, the proportion of nitrogen-rich stars in the Milky Way's GCs seems to be higher than astronomers expected. This suggests that a large chunk of the first-generation star population is missing. One fair explanation that astronomers have adopted is that clusters once contained many more stars but a large fraction of the first-generation stars were ejected from the cluster at some time in its past. In our galaxy, these stars could go to the halo.

Now, the observations of the Globular Cluster in Fornax contradict this hypothesis since they have found that the proportion of second-generation stars is quite similar to that of the GCs in the Milky Way, but unlike our galaxy, Fornax doesn't have enough old stars to account for the huge number that would have been banished from the clusters, and we should be able to see them but we don't.

These types of findings mean that a leading theory on how these mixed-generation globular clusters formed cannot be correct and astronomers will have to reconsider how these mysterious objects, in the Milky Way and further afield, came to exist.

As mentioned by Roueff et al. 1997, there is widespread belief that globular clusters cannot contain large amounts of dark matter, because of the observational results wouldn't match the Virial Theorem. This theorem relates the velocity dispersion σ (that we introduced before) at the center of the cluster to the total mass M_t and to the half-mass radius r_h of the system. For a one component globular cluster (no dark matter), that relation may be expressed as (Spitzer 1987):

$$\langle \sigma^2 \rangle \approx 0.4 \frac{GM_t}{r_h} \quad (2.1)$$

The use of the virial theorem to find the mass of a Globular Cluster could be a first approximation but it lacks of precision that could be acquired using more elaborated procedures involving the presence of dark matter. The mass modelling of these objects is still being debated since the existence of dark matter in the clusters is a mystery and further work (including the effects of the stellar populations) needs to be done to clarify the scenario and give us a stronger idea on how these objects and galaxies form.

Regarding the stellar populations, we note that these structures were once thought to consist of a single population of stars that all formed together. However, research has since shown that many of the Milky Way's globular clusters have far more complex formation histories and are made up of at least two distinct populations of stars [15]. A way of analysing the stellar populations in GCs is to use Colour-Magnitude diagrams. These diagrams plot the apparent magnitudes of the stars in a cluster against their colour indices. Globular Clusters nearly all have very similar colour-magnitude diagrams.

This diagram for a typical globular cluster looks very different than that of an open cluster. There are no Main Sequence stars of types OBAF, but there are many red giants. The brightest stars in a globular cluster are those at the tip of the red giant branch in the color-magnitude diagram, which explains the red appearance of the bright stars in color images of the clusters. You can also see stars populating the horizontal branch (and also why it is called the horizontal branch), the asymptotic giant branch, and even some stars that have colors and magnitudes of F stars, but far fewer than the G stars just below and to the right of them on the Main Sequence. In order to see the characteristics of these diagrams, figures 2.7 and 2.8 show the difference between the color-magnitude diagram of a typical globular cluster (M55 in this case) and that of generic stars outside GCs.

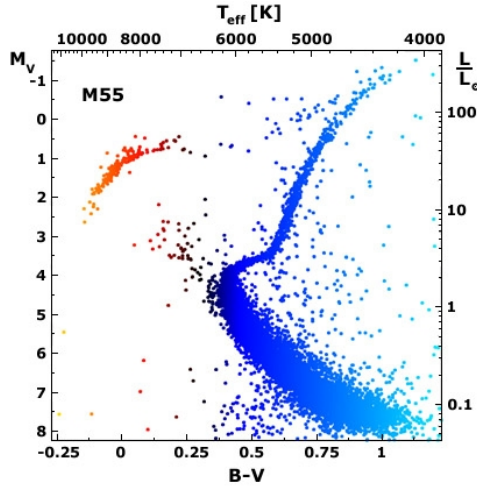


FIGURE 2.7: Color Magnitude diagram of M55 Globular Cluster. Over time, higher mass stars have evolved off the main sequence into red, then blue giants and beyond. The exact position of the sharp turn-off from the main sequence to the red giant branch measures the cluster’s age. Image by NASA.

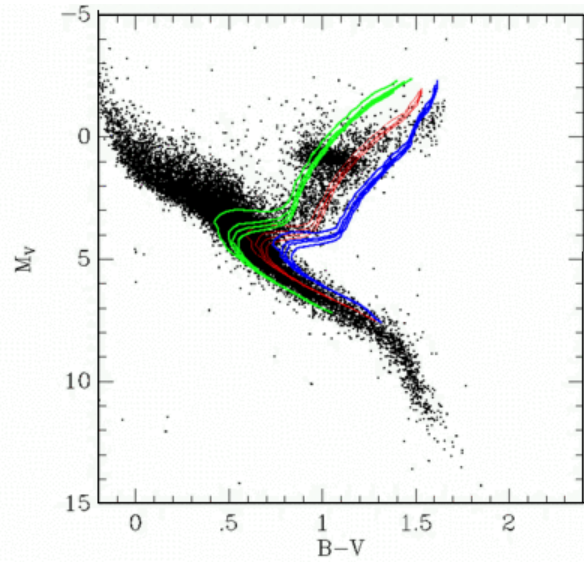


FIGURE 2.8: Colour magnitude diagram for nearby stars, with 3 isochrones of differing age overlaid (and four different metallicities each). The oldest stars in the disk have ages of about 10 Gyr. Source preprint. Jimenez, Flynn & Kotoneva, 1998.

Of the GC’s stellar populations, around half the stars are a single generation of normal stars that were thought to form first, and the other half form a second generation of stars, which are polluted with different chemical elements. In particular, the polluted stars contain up to 50100 times more nitrogen than the first generation of stars.

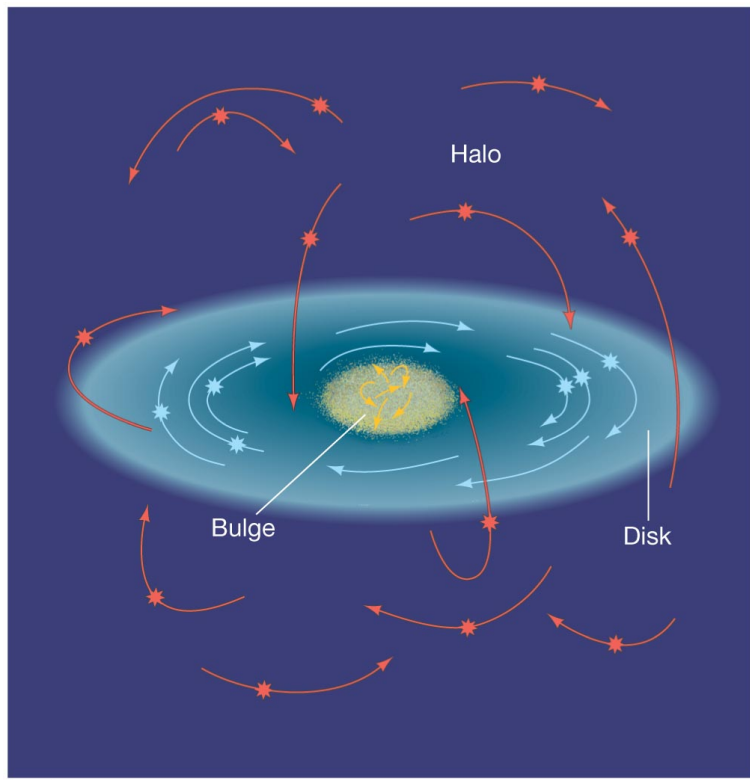
The proportion of polluted stars found in the Milky Way’s globular clusters is much higher than astronomers expected, suggesting that a large chunk of the first-generation star population is missing. A leading explanation for this is that the clusters once contained many more stars, but a large fraction of the first-generation stars were ejected from the cluster at some time in its past.

In the past, we didn’t know whether globular clusters in smaller galaxies had multiple stellar generations or not, but recent observations show clearly that they do [15]. This finding means that a leading theory on how these mixed-generation globular clusters formed cannot be correct, and astronomers will have to think once more about how these mysterious objects in the Milky Way and further afield came to exist.

The other fundamental observational procedures to study GC’s are Radial velocity measurements that have revealed that most Globular Clusters are moving in highly eccentric elliptical orbits that take them far outside the Milky Way; they form a halo of roughly spherical shape which is highly concentrated to the Galactic Center, but reaches out to a distance of several thousands of parsecs, much more than the dimension of the Galaxy’s

disk. As they don't participate in the Galaxy's disk rotation, they can have high relative velocities of several 100 km/s with respect to our Solar System; this is what shows up in the radial velocity measurements.

We could picture their orbits as shown in figure ——.



Copyright © 2008 Pearson Education, Inc., publishing as Pearson Addison-Wesley.

FIGURE 2.9: Illustration of the orbits of some Globular Cluster in a spiral galaxy like the Milky Way. Picture from the Oregon University webpage

Now, when we talk about the observational properties of GCs, we must mention photometric and spectroscopic observations of individual stars in the Clusters, which can be achieved since the clusters are not too far away for our observations to be imprecise. In the context of dynamics, recursive photometric observations of cluster members can in principle give us information about their proper motion in the plane of sight, in addition to radial velocities, we could reconstruct their 3D velocity profile and the overall rotation of the clusters.

Individual spectroscopic observations, on the other hand, can be very useful for reconstructing the velocity dispersion profile of the cluster. This can be made using the doppler shift of the spectral lines in the spectra, by cross correlating the observed spectra with a rest frame spectrum and measuring the projected radial velocity of the stars, result of the cross correlation. The mathematical treatment that has to be done to infer

the velocity dispersion profile and obtaining information about the potential well is well described in the next section.

For elliptical galaxies, and thus globular clusters, the **surface brightness** usually follows a Sersic profile of the form:

$$I(R) = I_e e^{-b_n \left[\left(\frac{R}{R_e} \right)^{1/n} - 1 \right]} \quad (2.2)$$

where I_e is the intensity at the effective radius R_e that encloses half of the total light from the model (Caon et al. 1993). For the special case of $n = 4$ we have the De Vaucouleurs profile:

$$I(R) = I_e e^{-7.669 \left[\left(\frac{R}{R_e} \right)^{1/4} - 1 \right]} \quad (2.3)$$

That we shall use to find the effective radius in our modelling using the observational data.

2.4 ω Centauri

2.5 Mass models and Dynamics

In order to get into the physical discussions about the equilibrium and modelling of globular clusters, we need to understand first the basics of potential theory, and more specifically the potential theory of spherical systems. The next step is to discuss the physical conditions of equilibrium of these models so that the mass modelling can be made. The last but most important part is to discuss the criteria regarding the mathematical treatment of the dynamics of these systems in the context of the collisionless Boltzmann equation and the approximations to the solutions of the Jeans equations that will be used for the fitting of the observational data to do the final modelling.

2.5.1 Potential Theory of Spherical Systems

Our discussions about Potential Theory for large stellar systems will be studied using the simplifications given by the spherical symmetry of globular clusters. We first introduce some of the most important theorems for calculating the gravitational potential of a spherically symmetric distribution of matter provided by Newton, these theorems

are physically related to Gauss theorem and may be proved using simple geometric assumptions or using a more precise results from vectorial calculus.

Newton's first theorem states that a body that is inside an uniform spherical shell of matter experiences no net gravitational force from that shell.

Newton's second theorem states that the gravitational force on a body that lies outside a spherical shell of matter is the same as it would feel if all the shell's matter were concentrated into a point at its center.

It follows from Newton's theorems that the gravitational force of a spherical density distribution $\rho(r')$ on a unit mass at radius r is entirely determined by the mass interior to r is given by

$$\mathbf{F}(r) = -\frac{GM(r)}{r^2} \hat{\mathbf{e}}_r \quad (2.4)$$

Where the mass as a function of the radius is

$$M(r) = 4\pi \int_0^r dr' r'^2 \rho(r') \quad (2.5)$$

We can consider that the total gravitational potential of the spherical system is the sum of the potentials given by spherical shells of a differential mass $dM(r) = 4\pi\rho(r)r^2dr$. This way, we may calculate the gravitational potential at \mathbf{r} generated by a spherically symmetric density distribution $\rho(r')$ by adding the contributions to the potential produced by shells with $r' < r$, and with $r' > r$. Thus we obtain

$$\begin{aligned} \Phi(r) &= -\frac{G}{r} \int_0^r dM(r') - G \int_r^\infty \frac{dM(r')}{r'} \\ &= -4\pi G \left[\frac{1}{r} \int_0^r dr' r'^2 \rho(r') + \int_r^\infty dr' r' \rho(r') \right] \end{aligned} \quad (2.6)$$

We note an important property of a spherical matter distribution regarding its circular speed $v_c(r)$, defined to be the speed of a particle of negligible mass in a circular orbit at radius r . We may evaluate v_c by equating the gravitational attraction $|\mathbf{F}|$ to the centripetal acceleration v_c^2/r :

$$v_c^2 = r|\mathbf{F}| = r \frac{d\Phi}{dr} = \frac{GM(r)}{r} \quad (2.7)$$

We may also note that the **escape speed** v_e in terms of the gravitational potential is

$$v_e(r) \equiv \sqrt{2|\Phi(r)|} \quad (2.8)$$

The **potential energy of spherical systems** comes from a very general equation, also in terms of the potential:

$$W = - \int d^3x \rho x \cdot \nabla \Phi \quad (2.9)$$

By substituting equation (2.1) and integrating over all directions of \mathbf{r} we get:

$$W = -4\pi G \int_0^\infty r dr \rho(r) M(r) \quad (2.10)$$

The potential energy tensor of a spherical body is **diagonal** i.e it is isotropic, and has the form:

$$W_{jk} = \frac{1}{3} W \delta_{jk} \quad (2.11)$$

Once we have the general results for the potential of spherical distributions we can move on to study special cases, let's study potential-density pairs that would best fit for Globular Clusters.

The simplest model is the **homogeneous sphere** of radius a , characterized by the gravitational radius $r_g \equiv GM^2/|W|$, with $r_g = \frac{5}{3}a$, for which the gravitational potential is:

$$\Phi(r) = \begin{cases} -2\pi G\rho \left(a^2 - \frac{1}{3}r^2\right) & (r < a) \\ -\frac{4\pi G\rho a^3}{3r} & (r > a) \end{cases} \quad (2.12)$$

For spherical systems, the density is roughly constant near the center, and falls to zero at large radii. A potential of a system of this type would be proportional to $r^2 + \text{constant}$ at small radii and to r^{-1} at large radii. The **Plummer Model** is a simple potential with these properties and it is of the form

$$\Phi = -\frac{GM}{\sqrt{r^2 + b^2}} \quad (2.13)$$

Where M represents the total mass of the system and b is called the **Plummer scale length** which characterises this model to a simple homogeneous sphere model. From this potential, using spherical coordinates we can calculate the laplacian ∇^2

$$\nabla^2\Phi = \frac{1}{r^2} \frac{d}{dr} \left(r^2 \frac{d\Phi}{dr} \right) = \frac{3GMb^2}{(r^2 + b^2)^{5/2}} \quad (2.14)$$

And from $\nabla^2\Phi = 4\pi G\rho$ (**Poisson's equation**) the corresponding density to the potential:

$$\rho(r) = \frac{3M}{4\pi b^3} \left(1 + \frac{r^2}{b^2} \right)^{-5/2} \quad (2.15)$$

And finally the potential energy of a Plummer model is

$$W = -\frac{3\pi GM^2}{32b} \quad (2.16)$$

In 1911 Plummer used this potential-density pair to fit observations of Globular Clusters since it gets rid if the indetermination that would arise when $b \rightarrow 0$.

Another useful model is given by the **Isochrone Potential**, that gives analytic orbits to all the stars orbiting the system (For a Plummer potential the position of a star orbiting the system cannot be given in terms of elementary functions). This model is of the form

$$\Phi(r) = -\frac{GM}{b + \sqrt{b^2 + r^2}} \quad (2.17)$$

By Poisson's equation the density associated with the isochrone potential is:

$$\rho(r) = \frac{1}{4\pi G} \frac{1}{r^2} \frac{d}{dr} \left(r^2 \frac{d\Phi}{dr} \right) = M \left[\frac{3(b+a)a^2 - r^2(b^2 + 3a)}{4\pi(b+a)^3 a^3} \right] \quad (2.18)$$

So that in the extreme cases the isochrone potential yields:

$$\rho(r) = \begin{cases} \frac{3M}{16\pi b^3} & (r = 0) \\ \frac{bM}{2\pi r^4} & (r \gg b) \end{cases} \quad (2.19)$$

As a very useful approximation, we can work with **Two-power density models**. First, we note that the luminosity density of many elliptical galaxies can be approximated as a power law in radius at both the largest and smallest observable radii, with a smooth

transition between these power laws at intermediate radii. Some numerical simulations of the clustering of dark matter particles suggest that the mass density within a dark halo has a similar structure. This is the reason for which much attention has been given to models with a density of the form:

$$\rho(r) = \frac{\rho_0}{(r/a)^\alpha (1+r/a)^{\beta-\alpha}} \quad (2.20)$$

Dark matter halos are often modelled by the above equation with $\beta \simeq 3$ and α in the range (1, 1.5). Dehnen models are the solutions for $\beta = 4$ that have simple analytic properties. But we may discuss some specific results summarized in the following table:

| Model | α | β |
|------------------|----------|---------|
| Hernquist (1990) | 1 | 4 |
| Jaffe (1983) | 2 | 4 |
| NFW (1995) | 1 | 3 |

TABLE 2.1: Two-power density potentials given by the different values of α and β

Navarro, Frenk, & White (1996) showed that the values taken by the free parameters α and β for the halos that formed in their simulations were strongly correlated, so the halos were essentially members of a one-parameter family.

According to equation (2.17) the mass inside the radius r is:

$$M(r) = 4\pi\rho_0 a^3 \int_0^{r/a} ds \frac{s^{2-\alpha}}{(1+s)^{\beta-\alpha}} \quad (2.21)$$

For the important cases we discuss, the mass is

$$M(r) = 4\pi\rho_0 a^3 \times \begin{cases} \frac{r/a}{1+r/a} & \text{for a Jaffe model} \\ \frac{(r/a)^2}{2(1+r/a)^2} & \text{for a Hernquist model} \\ \ln(1+r/a) - \frac{r/a}{1+r/a} & \text{for a NFW model} \end{cases} \quad (2.22)$$

We can directly integrate the mass to get the potential for the three discussed models:

$$\Phi(r) = -4\pi G \rho_0 a^2 \times \begin{cases} \ln(1+r/a) & \text{for a Jaffe model} \\ \frac{1}{2}(1+r/a)^{-1} & \text{for a Hernquist model} \\ \ln(1+r/a)(r/a)^{-1} & \text{for a NFW model} \end{cases} \quad (2.23)$$

As will be mentioned in the modelling chapter, we focus on the Hernquist model and make some modifications on it. In order to introduce the model as done by Lars Hernquist in 1989 with his “An analytical model for spherical galaxies and bulges” let’s start by considering the density profile that resembles a $R^{1/4}$ (de Vaucouleurs) at small radii

$$\rho(r) = \frac{M}{2\pi} \frac{a}{r} \frac{1}{(r+a)^3} \quad (2.24)$$

Where a is the scalength and M is the total mass of the distribution. The cumulative mass distribution corresponding to this density profile is

$$M(r) = M \frac{r^2}{(r+a)^2} \quad (2.25)$$

And the potential takes the form

$$\phi(r) = -\frac{GM}{r+a} \quad (2.26)$$

Now, the projected surface brightness in the Hernquist model in terms of the mass-to-light ratio Γ and the projected radius R is:

$$I(R) = \frac{M}{2\pi a^2 \Gamma (1-s^2)^2} [(2+s^2) X(s) - 3] \quad (2.27)$$

where $s = R/a$, R is the projected radius and:

$$X(s) = \frac{1}{\sqrt{1-s^2}} \operatorname{sech}^{-1} s \quad \text{for} \quad 0 \leq s \leq 1 \quad (2.28)$$

$$X(s) = \frac{1}{\sqrt{s^2-1}} \operatorname{sec}^{-1} s \quad \text{for} \quad 1 \leq s < \infty \quad (2.29)$$

We will come back to these equations in chapter 4 where we do the modelling and the modifications to Hernquist profile.

The next step in the analysis of the dynamics of Globular Clusters is to understand the physics of spherical distribution of systems and how the solutions for their equilibrium dynamics can be easily reached. As we shall see, a good consideration for the simplification of the mathematical treatment of Globular Clusters (with good physical reasons) is that these systems are not collisional.

2.5.2 Collisionless Systems

The problem of modelling the structure and dynamics of Globular Clusters is not trivial whatsoever. Several assumptions and physical approaches need to be made to simplify the problem and reach results that fit the observational data. One of the main assumptions is that the stellar systems that we will study are **collisionless**. This assumption not only reduces the problem of determining the functional form of the position and velocities of the stars but also has strong physical reasons that must be mentioned.

In the context of stellar systems, collision refers to any interaction between individual particles, such as direct encounters, gravitational assistance, sudden disruption of the orbit, or any interaction that changes the stars orbit in a significant way. That the system is collisionless means that it is a system in which the interaction cross-section between particles (stars in this case) is so low that collisions between particles have no significant effect on the system so that the dominant component of the dynamics is the potential well produced by the system as a whole.

One of the other approximations we make is that the orbits of stars in the system can be determined by assuming that the mass of the Globular Cluster is distributed smoothly in space, rather than concentrated in certain positions as point masses. The true orbits deviate significantly from this approximated model, but in systems with more than a few thousand stars like a globular cluster (that can easily reach hundreds of thousands or millions of stars), the deviation is small and the potential and mass distribution can be approximated as continuous functions.

As a star moves through a stellar system, it will feel the gravitational force due to all other stars. We want to determine if the motion of the stars is mainly determined by the average gravitational force of all other stars combined, or if it is mostly sensitive to the force due to nearby stars, in order to do this we must refer to some parameters of time that we properly define like **relaxation** and **crossing** time.

Relaxation time refers to the time that is necessary for the particles (stars) in the system to change significantly their velocity, so that they lose all memory of their initial orbits. In other words, it is the time taken for the cumulative effect of chance encounters between stars to be so great that the actual orbit of a star cannot be described, even approximately, by the theoretical orbit which is derived by ignoring chance encounters and considering only the effect of the smoothed-out distribution of mass in the system (D. Asoka Mendis, 1970).

The other fundamental parameter we need to define is the crossing time which refers to the typical time that would take to a star to cross the whole system, in terms of the size of the system r and the velocity v of the stars, this time is:

$$t_{cross} = \frac{r}{v} \quad (2.30)$$

The relaxation time in terms of the crossing time and the number of stars N is:

$$t_{relax} = \frac{N}{8\ln(N)} t_{cr} \quad (2.31)$$

As these quantities parametrize the interactions between stars, their values really give us a strong idea on how the dynamics can be modelled, as it was mentioned before, for a typical Globular Cluster, the evolution time t_{evo} is usually much larger than the relaxing time which is much larger than the crossing time, so the effects of the interaction between stars is minimal and we can use the approximation that the system is collisionless.

$$t_{cross} \ll t_{relax} \ll t_{evo} \quad (2.32)$$

2.5.3 Dynamics

Using the approximations we just mentioned, the dynamics of stars in Globular Cluster Systems can be solved assuming that those stars are moving under a smooth potential $\phi(x, y, z, t)$ and that at any time t a full description of the state of these systems is given by specifying a function of the number density of stars with their position and velocities $f(\vec{x}, \vec{v}, t)$ which is called the distribution function of phase space density because it is given in the phase space. This function is the number of stars in volume $d\vec{x}$ with velocities in range $d\vec{v}$ (centered on \vec{x}, \vec{v}).

This flow of points (or stars) of f is incompressible in the phase space (the density remains conserved along a flow-line) so that

$$\frac{df}{dt} = 0 \quad (2.33)$$

To infer properly the equation above and understand the time evolution, we define a coordinate \vec{w} for the stars in phase space:

$$\vec{w} \equiv (\vec{x}, \vec{v}) \equiv (w_1, w_2, \dots, w_6) \quad (2.34)$$

The flow of the star is given by

$$\dot{\vec{w}} = (\dot{\vec{x}}, \dot{\vec{v}}) = (\vec{v}, -\vec{\nabla}\Phi) \quad (2.35)$$

The flow $\dot{\vec{w}}$ conserves stars so we have the continuity equation:

$$\frac{\partial f}{\partial t} + \sum_{\alpha=1}^6 \frac{\partial(f w_\alpha)}{\partial w_\alpha} = 0 \quad (2.36)$$

Using the chain rule for w our continuity equation explicitly in terms of the position and velocities is:

$$\frac{\partial f}{\partial t} + \sum_{i=1}^3 \frac{\partial f}{\partial x_i} \dot{x}_i + \sum_{i=1}^3 \frac{\partial f}{\partial v_i} \dot{v}_i = 0 \quad (2.37)$$

It is more useful to use the derivative of the velocity in terms of the potential with the relation $\dot{v}_i = -\partial\phi/\partial x_i$ as:

$$\frac{\partial f}{\partial t} + \sum_{i=1}^3 \frac{\partial f}{\partial x_i} v_i - \sum_{i=1}^3 \frac{\partial f}{\partial v_i} \frac{\partial\phi}{\partial x_i} = 0 \quad (2.38)$$

or

$$\frac{\partial f}{\partial t} + \nabla f \cdot \vec{v} - \frac{\partial f}{\partial \vec{v}} \cdot \nabla\phi = 0 \quad (2.39)$$

These equations are the Collisionless Boltzmann Equations (CBE) and they are sufficient to study the evolution of the distribution function f with time. As the CBE is a very complicated equation of 7 variables, its solution is a challenging task and some assumptions and creative methods have been developed for its solutions, one of them refers to the moments of the distribution function and the other is based on the Jeans theorem.

The moments approximation consists of considering that if the dependence of the phase space density upon velocity is relatively smooth and free of singularities, one can collapse the 6-dimensional phase space density into a set of functions of 3-dimensional position by taking moments of the velocities. First, let's note that the moment of order j of the distribution f is

$$\overline{x^j} = \frac{\int x^j f dx}{\int f dx} \quad (2.40)$$

We can define functions for the characterization of the distribution function on terms of one of its variables:

$$\nu(\vec{x}) \equiv \int f(\vec{x}, \vec{v}) d^3 v \quad \text{or} \quad \xi(\vec{x}) \equiv \int f(\vec{x}, \vec{v}) d^3 x \quad (2.41)$$

So that the zeroth moment of the velocity is just the number density $\nu(\vec{x})$ and for each of three velocity components the first moment gives a mean velocity:

$$\bar{v}_i(\vec{x}) \equiv \frac{1}{\nu(\vec{x})} \int v_i f(\vec{x}, \vec{v}) d^3 \vec{v} \quad (2.42)$$

Likewise, we can define higher order moments with combinations of powers of the three velocity components. The second moments give a really important and useful quantity related to the **velocity dispersion tensor** σ_{ij}^2

$$\bar{v}_i \bar{v}_j(\vec{x}) \equiv \frac{1}{\nu(\vec{x})} \int v_i v_j f(\vec{x}, \vec{v}) d^3 \vec{v} = \sigma_{ij}^2 + \bar{v}_i \bar{v}_j \quad (2.43)$$

The velocity dispersion tensor which will be fundamental in the mass modelling is thus defined as:

$$\sigma_{ij}^2 = \bar{v}_i \bar{v}_j - \bar{v}_i \bar{v}_j \quad (2.44)$$

There is quite some observational support that ideally the velocity distribution functions are reasonably well described by the low order moments; a density and a set of low order moments may therefore give a reasonably complete description of a collisionless system.

Now to find the Jeans equations and show a different approach for the solution of the CBE we need to manipulate the results for the moments of the DF. By multiplying the CBE by powers of the velocity components, and integrating over velocity space we obtain a series of differential equations for the various velocity components on the zeroth moment, we have (using Einstein's notation of summation):

$$\int \frac{\partial f}{\partial t} d^3 \vec{v} + \int v_i \frac{\partial f}{\partial x_i} d^3 \vec{v} - \frac{\partial \Phi}{\partial x_i} \int \frac{\partial f}{\partial v_i} d^3 \vec{v} = 0 \quad (2.45)$$

Using the divergence theorem for the last term and replacing by the definitions of $\nu(x)$ and $\bar{v}_i\nu(x)$ we get:

$$\frac{\partial}{\partial t}\nu + \frac{\partial}{\partial x_i}(\nu\bar{v}_i) = 0 \quad (2.46)$$

Which looks just like a standard 3-D continuity equation. Now, we do the same procedure for the first moment, (again taking the spatial and temporal derivatives outside the velocity integrals) and integrating by parts and expressing the results in terms of our average velocities:

$$\frac{\partial}{\partial t}(\nu\bar{v}_j) + \frac{\partial}{\partial x_i}(\nu\bar{v}_i\bar{v}_j) + \frac{\partial\Phi}{\partial x_i} \int f \frac{\partial v_j}{\partial v_i} d^3\vec{v} = 0 \quad (2.47)$$

The last term on the left hand side becomes $\nu\delta_{ij}$ in an orthogonal coordinate system. So applying the product rule and our continuity equation to the first term we get

$$\nu \underbrace{\frac{\partial \bar{v}_j}{\partial t}}_{\text{acceleration}} - \bar{v}_j \underbrace{\frac{\partial}{\partial x_i}(\nu\bar{v}_j)}_{\text{viscosity}} + \underbrace{\frac{\partial}{\partial x_i}[\nu(\sigma_{ij}^2 + \bar{v}_i\bar{v}_j)]}_{\text{gravity}} = -\nu\bar{v}_i \underbrace{\frac{\partial\Phi}{\partial x_j}}_{\text{pressure}} \quad (2.48)$$

Where we used the relation between the second moments and the velocity dispersion, finally differentiating the second term on the left hand side, part of the result cancels part of the third term and we arrive to the **Jeans' equations** for a collisionless fluid

$$\underbrace{\nu \frac{\partial \bar{v}_j}{\partial t}}_{\text{acceleration}} + \underbrace{\bar{v}_i \nu \frac{\partial \bar{v}_j}{\partial x_i}}_{\text{viscosity}} = -\nu \underbrace{\frac{\partial\Phi}{\partial x_j}}_{\text{gravity}} - \underbrace{\frac{\partial}{\partial x_i}(\nu\sigma_{ij}^2)}_{\text{pressure}} \quad (j = 1, 2, 3) \quad (2.49)$$

One important use of the Jeans' equations is to calculate the number density and potential self-consistently, assuming a given model for the velocity dispersion.

The Jeans theorem states that any steady state solution of the CBE depends on the phase-space coordinates (x, v) only through integrals of motion in a static potential, and any function of the integrals yields a steady state solution of the CBE. The value of this theorem is that it gives us a way of closing the loop for solving the Boltzmann equation.

Finally, it is important to introduce a useful parameter called the **Anisotropy parameter** β which gives us information about the preferred directions of movement of the stars in the system, if there are any. In spherical coordinates the anisotropy parameter is defined as

$$\beta \equiv 1 - \frac{(\sigma_\theta^2 + \sigma_\phi^2)}{2\sigma_r^2} \quad (2.50)$$

If $\beta = 0$, then $\bar{v}_r^2 = \bar{v}_\phi^2 = \bar{v}_\theta^2$ and we have zero anisotropy (there are no preferred directions for the stars in the system and the velocity dispersion tensor is completely symmetric) as in the ideal case of a spherical system in equilibrium. On the other hand, when $\beta = 1$ we have that the system has total anisotropy.

In the context of the Jeans equations, the surface brightness $I(R)$ and the projected velocity dispersion σ_p can be set in terms of the luminosity density ν and the velocity dispersion \bar{v}_r^2 (Binney & Tremaine 1987). For the simplest case in which $\beta = 0$ we have

$$I(R)\sigma_p^2(R) = 2 \int_R^\infty \frac{\nu \bar{v}_r^2 r dr}{\sqrt{r^2 - R^2}} \quad (2.51)$$

And for a more general case with $\beta \neq 0$ and writing explicitly the mass-to-light ratio $\Gamma = \rho/\nu$ we have

$$I(R)\sigma_p^2(R) = \frac{2}{\Gamma} \int_R^\infty \left(1 - \beta \frac{R^2}{r^2}\right) \frac{\nu \bar{v}_r^2 r dr}{\sqrt{r^2 - R^2}} \quad (2.52)$$

Which is going to be a fundamental equation in this thesis since it is the starting point of our modelling and because it allows us to use the observational data of projected velocity dispersions in the cluster.

Finally, to set the basis of the dynamics of collisionless systems we show how the radial velocity dispersion is related to the gradient of the potential of the system. From the Jeans equations in spherical coordinates, and assuming $\partial/\partial\theta = 0$, $\partial/\partial\phi = 0$ and $\partial/\partial t = 0$ we have that the first moment is

$$\frac{d}{dr} (\rho \bar{v}_r^2) + \frac{\rho}{r} \left(2\bar{v}_r^2 - \bar{v}_\theta^2 - \bar{v}_\phi^2\right) + \rho \frac{d\phi}{dr} = 0 \quad (2.53)$$

If we take the velocity tensor to be isotropic, that is $\sigma_r^2 = \sigma_\phi^2 = \sigma_\theta^2$ then the last equation becomes

$$\frac{d}{dr} (\rho \sigma_r^2) + \rho \frac{d\phi}{dr} = 0 \quad (2.54)$$

So the radial velocity dispersion is of the form

$$\sigma_r^2 = \frac{1}{\rho(r)} \int_r^\infty \rho \frac{d\phi}{dr} dr \quad (2.55)$$

This is also a fundamental equation for our modelling as it depends on the potential-density pair that one chooses to model the observations of velocities and surface brightness of members of systems that we could approach to as collisionless.

Chapter 3

Observations and Analysis

In order to study this problem about the dynamics of Globular Clusters in our galaxy we need scientific data that allows us to build a model that fits our observations. Under supervision of professor Juan Carlos Muñoz Cuartas and with three other undergraduate students from the University of Antioquia a trip to the OPD (Pico dos Dias Observatory) was made to Brazil in May 2014, besides the observational experience of the students, the main purpose of the trip was to get important data for this project. We needed two sets of data corresponding to spectra and photometric images of different Globular Clusters

The spectroscopic data allows us to determine the relative motion of individual stars (in the case of individual spectra) to infer the velocity dispersion profile. The integrated spectra can give us information about the stellar populations and it can also be used to infer composite velocity dispersions due to the Doppler broadening of the spectral lines. The photometric data allows us to study the surface brightness distribution for them. We can use all of this information to infer the properties of the globular clusters' mass distribution in order to build complete dynamical models and therefore infer the amount of dark matter present in the globular clusters (if there is any).

3.1 Observational Procedures

Our stay in OPD consisted of two days in the main dome for the spectroscopic data (using the Perkin-Elmer (P&E) telescope with a 1.6m mirror and the Cassegrain Spectrograph) and four days in a smaller dome for the photometric data in the IAG telescope with a 0.6m mirror. Figure 3.1 shows the configuration of telescopes in the observatory.



FIGURE 3.1: OPD observatory seen from the air, the big dome was used for the spectroscopic data and the small dome at the low right part of the photo for the photometric data.

3.1.1 Spectroscopic Data

The first two days (May 14th and 15th) we took the spectroscopic data in the telescope P&E with a diameter of 1.6m. The main instrument was the Cassegrain spectrograph with a CCD Ikon-L camera and Filters UBVRI. The control software we used was the recently installed software TCSPD which is built in a LabView environment for Windows (2010). Figure 3.2 shows the telescope from inside the dome.



FIGURE 3.2: Perkin-Elmer telescope in the main dome in OPD used for the spectroscopic observations

We made the observations of dome flats, bias frames, comparison lamp frames, calibration stars, some galaxies and certain globular clusters of the milky Way organized by the best observation times using Simbad and Stellarium for the estimations of the coordinates and times respectively. The objects we observed in OPD are organized in Table 3.1.

| Object | α | δ | 14 th | 15 th | 16 th | 18 th | 19 th |
|---------|----------------|--------------|------------------|------------------|------------------|------------------|------------------|
| NGC5020 | 13h 12m 39.87s | +12°35'59.0" | ✓ | ✗ | ✗ | ✗ | ✗ |
| NGC5272 | 13h 42m 11.62s | +28°22'38.2" | ✓ | ✓ | ✓ | ✗ | ✗ |
| NGC4833 | 12h 59m 33.92s | -70°52'35.4" | ✓ | ✗ | ✗ | ✗ | ✗ |
| NGC4590 | 12h 39m 27.98s | -26°44'38.6" | ✓ | ✓ | ✓ | ✗ | ✓ |
| NGC5139 | 13h 26m 47.28s | -47°28'46.1" | ✓ | ✓ | ✓ | ✓ | ✓ |
| NGC5286 | 13h 46m 26.81s | -51°22'27.3" | ✓ | ✓ | ✗ | ✗ | ✓ |
| NGC6752 | 19h 10m 52.11s | -59°59'04.4" | ✓ | ✗ | ✗ | ✗ | ✗ |
| NGC6397 | 17h 40m 42.09s | -53°40'27.6" | ✓ | ✓ | ✓ | ✗ | ✓ |
| NGC6723 | 18h 59m 33.15s | -36°37'56.1" | ✓ | ✓ | ✗ | ✓ | ✓ |
| NGC7615 | 23h 19m 54.44s | +08°23'57.9" | ✓ | ✗ | ✗ | ✗ | ✓ |
| NGC6541 | 18h 08m 02.36s | -43°42'53.6" | ✓ | ✓ | ✗ | ✓ | ✓ |
| NGC2802 | 09h 16m 41.41s | +18°57'48.8" | ✗ | ✓ | ✗ | ✗ | ✗ |
| NGC5024 | 13h 12m 55.25s | +18°10'05.4" | ✗ | ✓ | ✗ | ✗ | ✗ |
| NGC6362 | 17h 31m 54.99s | -67°02'54.0" | ✗ | ✓ | ✗ | ✗ | ✗ |
| NGC6502 | 18h 04m 13.68s | -65°24'35.7" | ✗ | ✓ | ✗ | ✗ | ✗ |
| NGC7078 | 21h 29m 58.33s | +12°10'01.2" | ✗ | ✓ | ✗ | ✓ | ✗ |
| NGC7099 | 21h 40m 22.12s | -23°10'47.5" | ✗ | ✓ | ✗ | ✗ | ✗ |
| NGC6970 | 20h 52m 09.46s | -48°46'39.8" | ✗ | ✗ | ✗ | ✗ | ✓ |
| NGC6541 | 18h 08m 02.36s | -43°42'53.6" | ✗ | ✗ | ✗ | ✗ | ✓ |
| NGC6715 | 18h 55m 03.33s | -30°28'47.5" | ✗ | ✗ | ✗ | ✗ | ✓ |
| HR4963 | 13h 09m 56.99s | -05°32'20.4" | ✓ | ✗ | ✗ | ✗ | ✗ |
| HR4468 | 11h 36m 40.91s | -09°48'08.1" | ✓ | ✓ | ✗ | ✗ | ✗ |
| HR7950 | 20h 47m 40.55s | -09°29'44.8" | ✗ | ✓ | ✗ | ✗ | ✗ |
| HR4961 | 13h 09m 45.28s | -10°19'45.6" | ✗ | ✗ | ✓ | ✗ | ✗ |
| HR6308 | 16h 59m 57.71s | -25°05'31.9" | ✗ | ✗ | ✗ | ✓ | ✓ |
| HR7964 | 20h 49m 20.54s | -18°02'09.1" | ✗ | ✗ | ✗ | ✓ | ✗ |
| HR6386 | 17h 12m 13.62s | -25°15'18.6" | ✗ | ✗ | ✗ | ✗ | ✓ |

TABLE 3.1: Observed objects in OPD observatory, column 1 is the name of the observed object, column 2 and 3 are the equatorial coordinates of the objects, columns 4, 5, 6, 7 and 8 are the observation dates, where the 14th and 15th were the days we observed the spectroscopic data and the rest of days we observed photometric data. The check mark indicates that the object was observed and ✗ indicates it was not observed. The details of the observations for each day are explained right ahead.

Our set up configuration for the spectrograph was the following:

On May 14th, a diffraction grating of 900 lines per mm, a CCD IkonL and the central wavelength for the observations of 8500 Angstroms (with possibility of rotation of the

slit 90, +45 and -45). We used the slit of 2.52" and obtained data for the globular clusters: NGC5020, NGC5272, NGC4833, NGC4590, NGC5139, NGC5286, NGC6752, NGC6397, NGC6723, NGC6715 and NGC6541 using exposition times of 600 and 900 seconds. We also observed the calibration stars: HR4963 and HR4468 with exposures of 7 and 5 seconds. As it was the first day, we needed to be very careful in calibrating our instruments on order to have the objects in the right focus, we also made the rotation of the slit to use all the diffraction angles of the observations and our comparison lamps were of Ne-Ar.

On May 15th, we used the slit of 3.0", and used a central wavelength of 5500 Angstroms. This time we observed the following objects: NGC2802, NGC5024, NGC4590, NGC5139, NGC5286, NGC5272, NGC6362, NGC6397, NGC6723, NGC6502, NGC6541, NGC7078, NGC7099, the stars HR4468 and HR7950. We used pretty much the same exposition times than the day before, this time though, our comparison lamps were of He-Ar.

3.1.2 Photometric Data

The photometric data was acquired in the next four days (from May 16th to May 19th) in the 0.6m IAG telescope in OPD. We used the Johnson system for the different filters which were easily shifted with the given software in the control computers. Figure 3.3 shows the telescope from inside the dome.

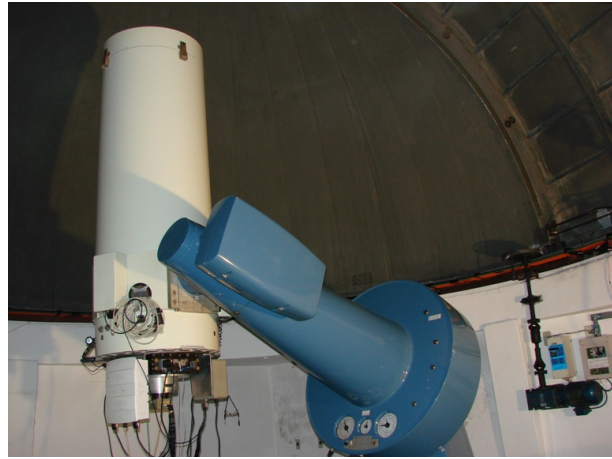


FIGURE 3.3: IAG telescope used for the photometric data

On May 16th, we took all the calibration images, consisting of 20 bias frames with an exposition time of 0,00001 seconds; also 22, 11, 11, 20 and 10 flat frames for the B,I,R,U,V filters respectively, their exposition times differed, for U filter we took various frames of 60 and 30 seconds, for the B filter we took frames of 30 seconds each, 15s for I, 60s for R and 3s for V. We took our "focus" images to calibrate the instrument,

and also various skyflats for all the filters. We targeted the following globular clusters and calibration stars in different filters: NGC5272, HR4961, NGC4590, NGC5139 and NGC6397. The exposition time for the clusters was of 600 seconds and 2 and 4 seconds for the calibration star.

May 17th was a terrible night for observations because the sky was too cloudy and the only useful data we could get were dome flats for the filters I,R and V that we could use instead of the bad dome flats of the first day. The reduction using the flats of another day are decent but this is not the ideal situation since mechanical movements of the instrument might slightly change its configuration and therefore it probably ends up with a reduction that is not the ideal one for science purposes.

On May 18th we were more organized since we were getting familiar with the observations and therefore the data we got had little trouble in the upcoming analysis, even though the sky was clody at the end of the night. The science objects we observed were NGC5139, HR6308, NGC6723, NGC6541, NGC7078, HR7964 that were observed in the different filters. We got 20 bias frames, 14 dome flats in the vaious filters, but no skyflats.

On May 19th we observed the Clusters NGC5139, NGC4590, NGC6723, NGC6715, NGC6541, NGC6970, NGC5286, NGC6397, NGC6541 and NGC6715, the calibration stars HR6386 and HR6308, 20 bias frames and flats for each filter.

It is important to mention that we had several tracking problems with the photometric data, and this affects the PSF of the photometry, the problems were due to a bad set up configuration of the telescope in OPD. Although we were able to get some decent data, for the most part the tracking problems made the stars look like ellipsoids thus making it hard for us to trust the photometric data for this thesis. Even though we did not use the data to its full potential, we explain the reduction and extraction procedures as a guide for the reader.

3.2 First step for Anaysis

Our first goal in starting the analysis of all the relevant data was to organize all the images in order to reduce the time required to make the reductions. For every day the calibrations images, trash, calibration stars and objects were separated and they were given their correct names as they were in the headers and compared with the information sheets we filled at the time we were doing the observations.

The next step was the reduction of all the images with the calibration files for each day, we started the photometric data to acquire certain skills in the use of IRAF because

the reduction of the spectroscopic data was a little more complex and needed a deeper understanding of IRAF packages.

We started with the cluster NGC-5139 (ω Centauri) because we got lots of data for that cluster in OPD and also because ω Centauri is a well known globular cluster since it is the largest in our galaxy and we can get a lot of information from the databases.

After the photometry of that cluster, the most relevant part of the reduction was to be made. The reduction and analysis of the spectroscopic data (May 14th and 15th), the methods for these reductions are quite special and are the most relevant part of the analysis because that is our most valuable information. The reduction was to be made very carefully because a good spectroscopic analysis depends upon a good reduction of the data. Just as with the photometric data, the first procedures were made for the Cluster NGC5139 to understand and master the techniques of the reduction and extractions.

3.3 Photometry

The photometry was made by the two traditional methods, PSF photometry and Aperture Photometry; even though the magnitudes calculated using both methods are quite different, the calibration constant between the two methods gave a good relation between them and made us trust the photometry results.

But first, the reduction of the data had to be done. The first step is to characterize the calibration images in order to see if there are any errors associated with the instrument or the way that the observations were made. By doing this we found that most of the flat-field images had brightness gradients in the corners and this was a problem we needed to correct because the increased value on the counts in these corners would affect the normalization of the super-flat that we would use to reduce the science data. Another systematic error that we found in all of our calibration and science frames was the presence of a strange water-looking figure at the top left corner of them, although it can be removed with the correct reduction, it obviously affected the CCD sensitivity by the time of the observations. Also, some filters showed a higher sensitivity to this systematic errors but at the end, the photometry could be made in the best data so that the dirty images don't affect our results.

In order to see how the data would be affected by the systematic errors we just mentioned, we produced a composite image using three images with the filters U,V and R and we did the same with the flats in those filters, the results are shown in figures 3.4 and 3.5.

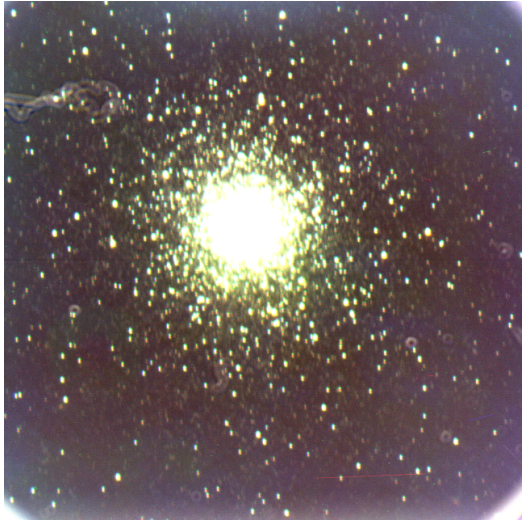


FIGURE 3.4: Composite image of NGC5139 in the U,V and R filters without being previously reduced, note that there is a significant amount of noise all over the image, specially in the borders. There is also a big strange object that might be a mote of dust in the top left corner.

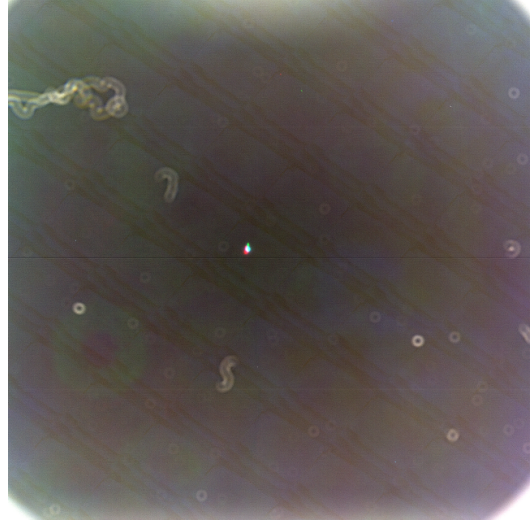


FIGURE 3.5: Composite image of the flats in the U,V and R filters showing the noise that needs to be extracted and which is present in all the filters, so that we can state that the mote-of-dust looking dirt and the border noise are a set up problem and not a problem for each single filter.

What we can infer from these images is that the flat fields and the bias frames contain the same noise that the science data thus giving us a good result in the reduction.

Once all the characterization is made we can reduce our important data using IRAF following the conventional steps consisting of:

- Building a Superbias: *Zerocombine* allows us to create the superbias using the median.
- Subtracting the Superbias to every flat and science data: We subtract the Superbias to every flat frame with no distinction on the filter, this is easily made using the task *imarith*, we also subtract them from the original science images.
- Building Superflats: It is necessary to create a Superflat frame for each filter because the response of the CCD and will be different for different wavelengths, we use the task *imcombine* to do this and this time we use the mode for better results.
- Divide the Superflats by the median: In order to normalize the flatfields we find the mode of each frame with *imstatistics* and then divide them by that value using *imarith*. An example of the normalized superflat at this point of the procedures is shown in figure 3.6.



FIGURE 3.6: Example of one of the Normalized Superflats in the I filter. This frame contains most of the noise that we want to extract from our science data because it contains background contamination and the instrumental noise such as motes of dust or imperfections in the instruments that could lighten or obscure the science data. Note that in the top left corner, the mote of dust looks very big and affects considerable a huge detection area and it must be removed using this normalized flat on the science frame.

- Reduce the science data: Finally, we divide the original images of the clusters and stars (with the bias subtracted) by the normalized Superflat to get the reduced images. This can easily be made using the task *imarith*.

3.3.1 Aperture Photometry

Now that the reduction has been made and the corrections pixel by pixel have been applied, we can proceed to do the photometry using the simplest technique, known as Aperture Photometry which consists of adding up the pixel counts within a circle centered on each star of the cluster and subtracting the quotient of the per-pixel average value of nearby sky count divided by the number of pixels within the aperture. This will result in the raw flux value of the target object. This Aperture Photometry was done using the task *Phot*:

For stars in ω Centauri, one must choose a very small aperture of the sky because the surrounding stars contribute to the flux that needs to be extracted and they are very close to each other, the crowded region of the center of ω Centauri is shown in figure 3.7.

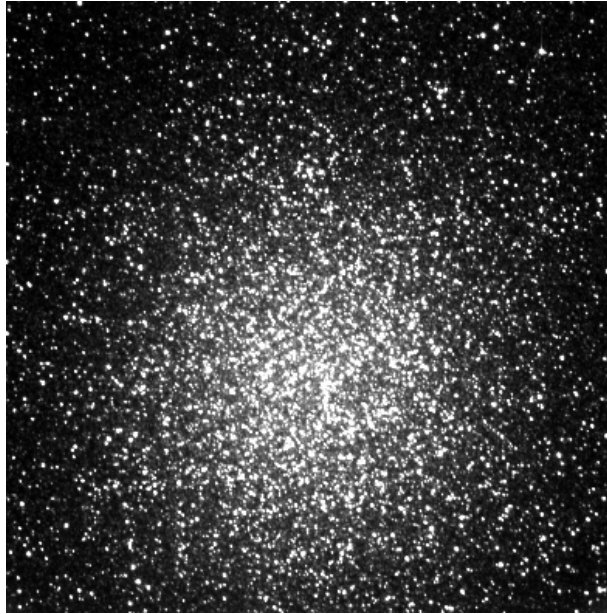


FIGURE 3.7: One of our reduced observations of ω Centauri in the V filter with an exposition time of 480 seconds. Note that the center of the cluster is too crowded so the photometry procedures must be done very carefully in order to reduce to the maximum the amount of noise that contributes to the stellar light contributions. The mote of dust in the top left corner (present in most of our observations) was successfully removed as it can be seen in this figure and it can now be used for aperture and PSF photometry.

With the task *imexamine* I find a value for the FWHM of 6.4 which I will use to set the size of the apertures to do the photometry. For the size of the aperture containing each star I chose an aperture size of four times the FWHM of the point spread function associated to the stars because it is the one that best fits the photometry and minimizes the error (calculated for some stars pressing “a” with the *imexamine* task) and for the width of the aperture I chose I value of 2.5 times the FWHM.

Another important value to take into account before editing the parameters in *phot* is the medium value of the background on the sky, in the case of this cluster, I do an average on many different places in the background of the image and find a value of sigma for the image that is equal to 53.45.

Now the photometry is done by changing some of the parameters including the readnoise and the gain. In the *fitskyparts* task inside *phot* I set the inner radius called *annulus* to be 25.6 (4FWHM) and the intermediate width called *dannulus* of 16 (2.5FWHM). Finally, before running the task I make sure I do the photometry using various apertures because I want to see which one minimizes the errors. I set apertures to be 1FWHM, 1.5FWHM, 2FWHM, 2.5FWHM, 3FWHM, 3.5FWHM and finally run the task. The results of the magnitude found for one of the star as a function of the size of the aperture is displayed in figure 3.8.

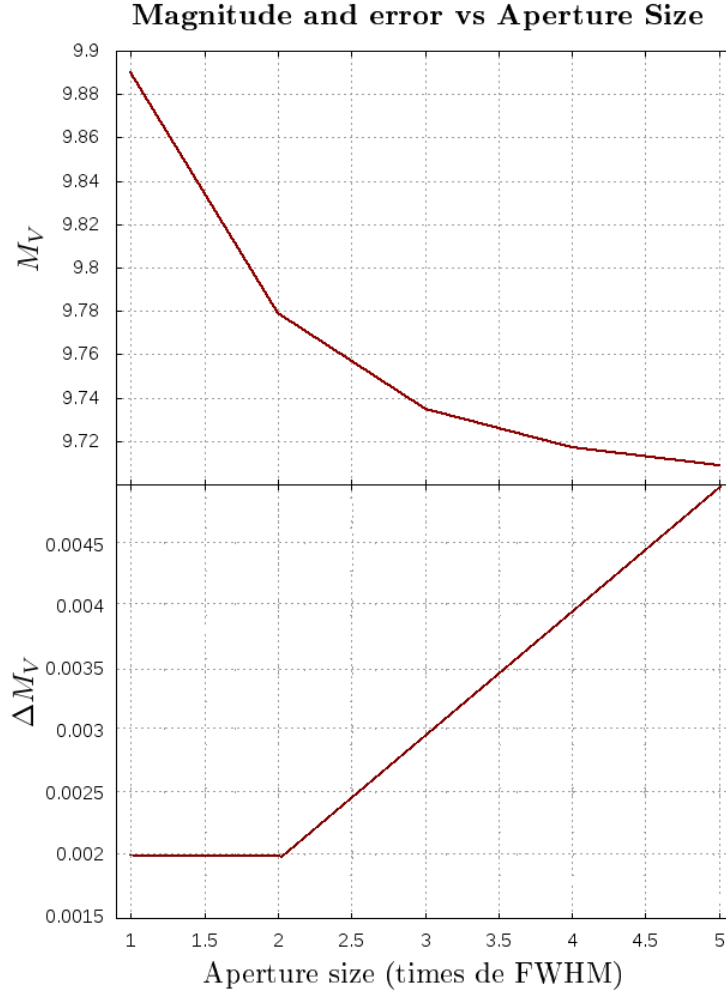


FIGURE 3.8: Magnitude dependence on the aperture size for the aperture photometry procedures. The X-axis are chosen in terms of the measured value of the FWHM. We note that while the magnitude decreases for bigger apertures, the associated error increases because the cluster is too crowded.

As we can see in figure 3.8, the magnitude of the chosen star in the cluster decreases for bigger apertures but the error increases because the space around the star is crowded with more stars and noise coming from the stars in the background so we infer that for crowded areas like this one the best choice is a small aperture. Although the results may not be as convincing, the use of another technique of photometry allows us to compare the results and see if the choice of a small aperture is a good way to fix or avoid the problem of the big noise of the background. For this purpose we use the technique of Point Spread Function (PSF) Photometry. Based on the manual “Creating a PSF for photometry with DAOPhot” by Dave Zurek, 1999.

3.3.2 PSF Photometry

There exist many ways to count photons for an image taken with a CCD camera, but all of these ways obey the same principle of energy distribution in luminous objects. The point spread function for each of these objects is an assigned measure from the probabilistic distributions that approach quite well to the count of photons that one wants to do in the photometric analysis of astronomical images. The PSF photometry technique advantage of the PSF of the objects using certain packages and tasks in a slightly different way than aperture photometry.

When doing photometry in a very crowded field, such as a globular cluster (ω Centauri in our case), where the profiles of stars overlap significantly, one must use de-blending techniques, such as point spread function (PSF) fitting, to determine the individual flux values of the overlapping sources because the noise of the background and the surrounding stars will always affect the aperture photometry in such a crowded cluster.

We selected our best data obtained in OPD to make a color-magnitude diagram of ω Centauri. Out of all the photometric images, we selected two images in the V and I band with exposition times of 480 seconds. We measured the instrumental magnitudes of thousands of stars in the cluster, by first doing the PSF modelling with some bright stars that were relatively isolated to surrounding stars in order to make the estimations more accurately.

First, by determining the FWHM of some of the stars and the standard deviation of the background, we can edit the parameters of the tasks *datapars*, *fitskypars* and *daofind* which are all included in the noao/digiphot/daophot package of IRAF. These values are found using the task *imexamine* on interactive mode with “a” for the FWHM of the stars and “m” for the standard deviation of the background.

After setting all the parameters of all of the individual tasks, we run *daofind* which will find the stars that match the criteria we mentioned above and will create a text file with the coordinates of those stars and will give to each star an ID.

The task *tmark* allows us to highlight the stars of the cluster in the display mode using the text file with the coordinates, and *txdump* allows me to put explicitly the coordinates of those stars in a text file that I use for the aperture photometry to make the first guess of the PSF of the stars.

The best way to correctly select the stars that will be used for the modelling of the PSF is by using the task *pstselect* that will select the stars that are well isolated using statistical techniques.

Once the stars are selected, the next step is to use the task *psf* which matches the point spread functions of the input images, by running this task, one can visualize how the PSF is modelled for each star and accept or decline the results to be stored, the interactive mode allows us to take the decision by analysing the modelling like the one we can see in figure 3.9 where it actually shown that the target star is saturated but has the proper behaviour of the Gaussian fit.

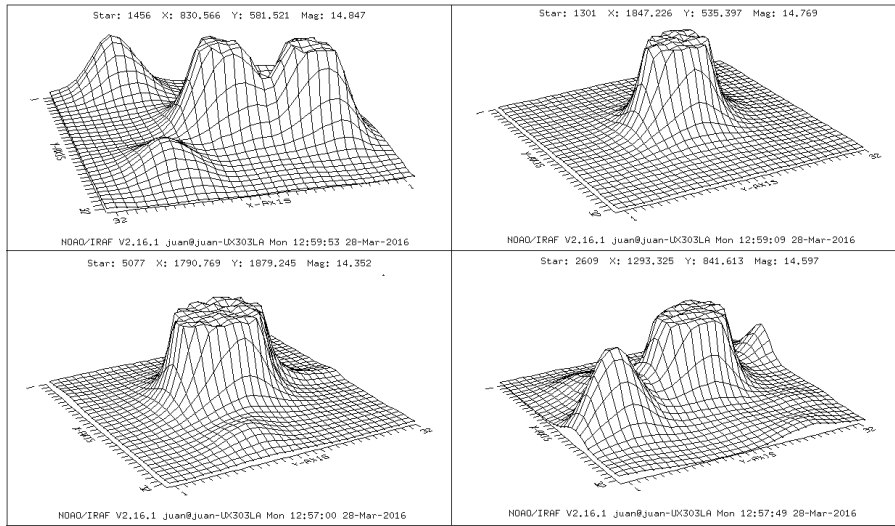


FIGURE 3.9: Some examples of the PSF modelling. The interactive mode allows us to accept or decline the result by pressing “a” or “d”. In the top left and bottom right panels, the PSF can’t be modelled correctly because they contain the contributions of various stars, the bottom left image is too saturated and is declined as well. The one at the top right has little noise and is the closest to a soft Gaussian behaviour (even though it is still a little saturated) so it can be accepted to model the PSF.

After running *psf*, there will be created an image that contains the residuals of the psf modelling which can be seen in figure 3.10.

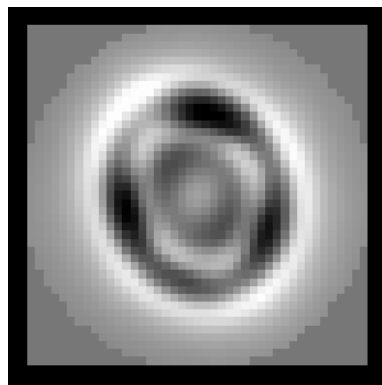


FIGURE 3.10: PSF residuals

With the task *seepsf* another image will be created but this time it will actually look like a star as shown in figure 3.11

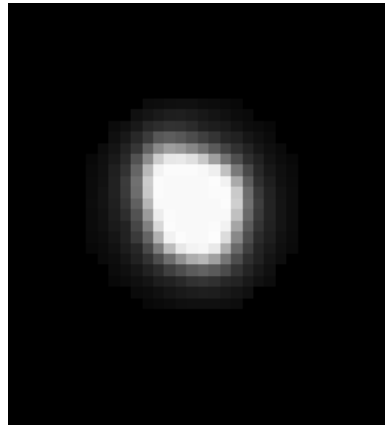


FIGURE 3.11: Seepsf converts a sampled PSF lookup table to a PSF image which can be visualized

Finally, after the modelling of the PSF was made, the task *allstar* does the photometry of the cluster using the results we just stored in the current directory. The results of the PSF photometry gave us magnitudes smaller for those stars than the results given by the aperture photometry but there is a constant difference for all the stars which we can assume to be a calibration constant between the two methods.

When the PSF photometry is ready for the two filters (I and V) we can use the tasks *tdump* and *tmatch* to extract the instrumental magnitudes for the H-R diagram.

Our color-magnitude diagram in the V and I bands is shown in figure 3.12.

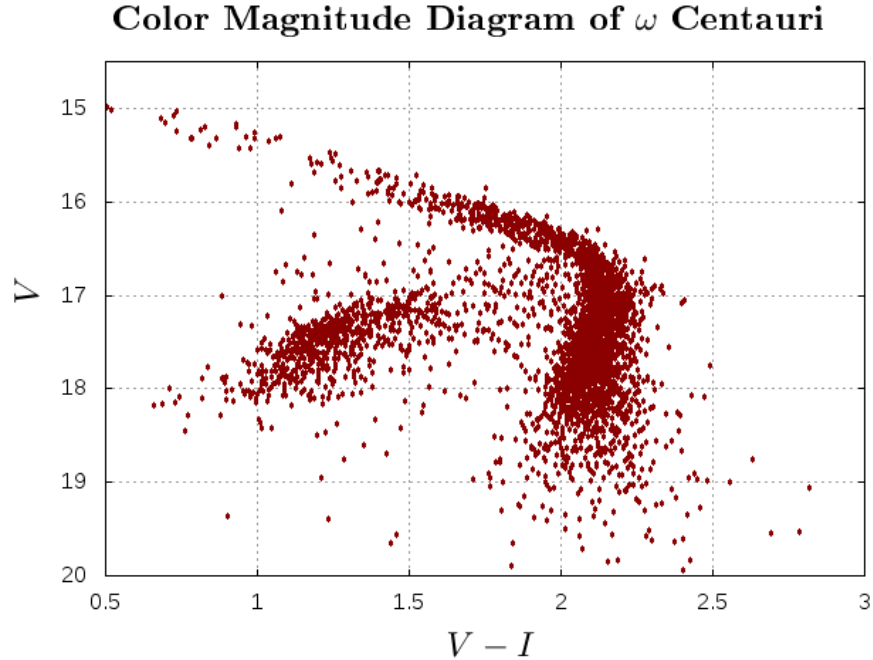


FIGURE 3.12: Color magnitude diagram of ω Centauri in the I and V bands made with OPD data observed on May 18th. The horizontal branch (HB) can be identified in the left crowded area of the diagram, as well as some stars belonging to the Turn off (TO) and main sequence (MS) regions in the bottom right of the diagram. The red giant branch should be in the top right region but it's not observed probably due to the saturation problems and the precision of the instrument used for the photometric data

3.4 Spectroscopy

This was the most important part of our observational data since it had the best quality we could obtain in the many domes of the observatory. Also, spectra of this kind is not easy to find in the scientific databases so we have important data to work with. The first spectroscopic procedures were also made for ω Centauri cluster since we need to master the reduction and extraction techniques first in order to be able to start the scientific work about the mass modelling of the clusters.

We based our reduction and extraction procedures on “A User’s Guide to Reducing Slit Spectra with IRAF”, by Phil Massey, Frank Valdes, and Jeannette Barnes, April 1992.

3.4.1 Spectroscopic Reduction

The spectroscopic reduction is made by following some steps taking into account that we did not take any Skyflats so we need to create a response function using our dome flats. The steps are:

- First we make a Superbias combining all the bias frames and then we subtract it from all the lamp, targets and flat field frames.
- It was important to analyse the flats to see which ones are saturated, we consider that values over 65,000 counts (using implot) show saturated data. The ones that we could trust for May 14th were ten images called flats_0012 to flats_0021.
- The pre-superflat is made using the median given the number of images.
- We need to make a trimming in all images because there are some regions in the images that show unexpected luminosity, this is probably due to border errors in the camera or the obturator time of relaxation. The zones we decided to cut (in pixels) were [0-100] and [575-691].
- A critical step is the creation of a response function, this is made by collapsing the pre-superflat to one column using *blkavg*. The useful image for the creation of the Superflat is done by combining this column with *blkrep*. This gives us an image that's uniformly distributed in the dispersion axis with the following IRAF commands.

```
blkavg MasterFlat.fits[1:475,*] AvgFlatCols 475 1
```

```
blkrep AvgFlatCols AvgFlatColsMaster 475 1
```

- The pre-superflat is now divided by the response function we created (AvgFlatCols-Master) and this gives us the Superflat that we will use to reduce our data.
- Finally, the task we use to remove the cosmic rays is *lacos*, and it gives very accurate results, as it shows the “mask” image with the removed cosmic rays.

Figures 3.13 and 3.14 show a dirty and a clean spectrum, where every strong vertical trace is the spectrum of a star. The vertical direction is the dispersion (in wavelength) of the spectrum and the horizontal direction is the spatial separation between stars. Note that there are some strong horizontal lines that span all the spatial direction of the spectrum even in the clean one, they are atmospheric lines that need to be considered in the wavelength and flux calibration of the spectra.

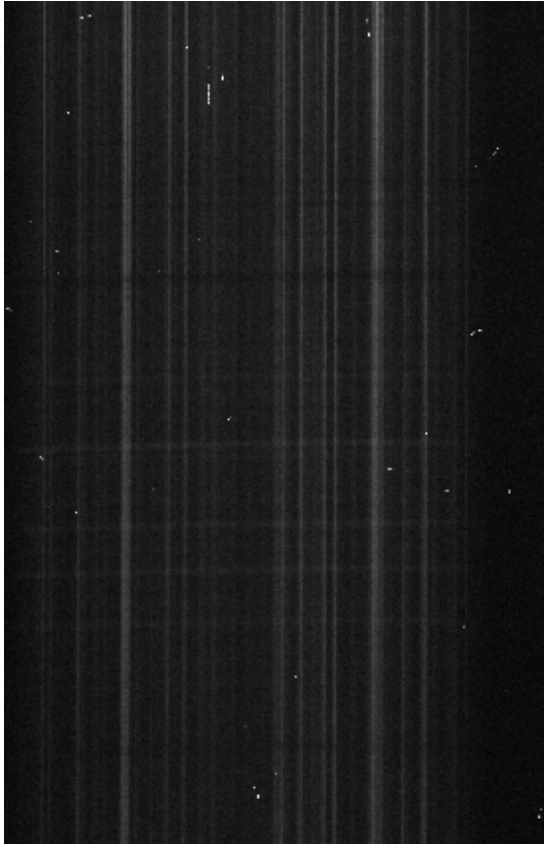


FIGURE 3.13: The dirty cluster spectrum has a small signal to noise ratio, besides border effects (such as a big gradient) that need to be trimmed and cosmic rays.

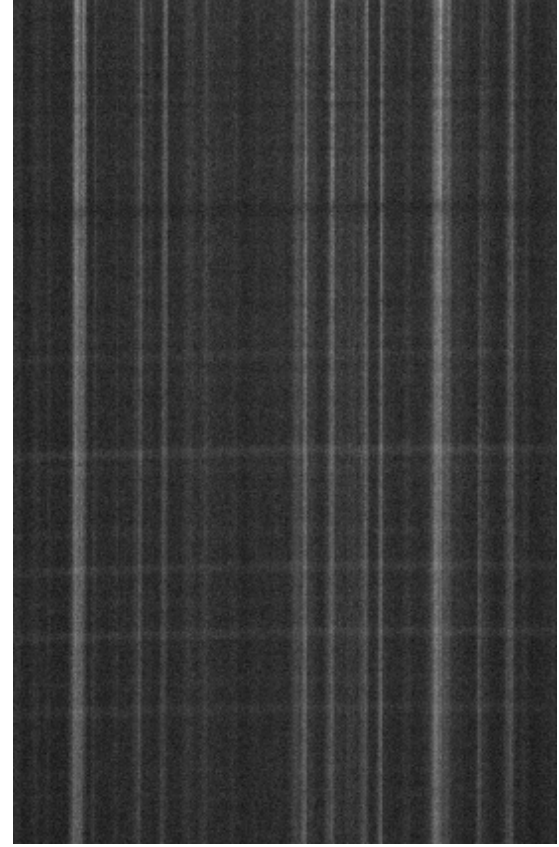


FIGURE 3.14: The clean spectrum without the bad data at the borders that needed to be trimmed, with a higher signal to noise ratio and the cosmic rays removed

The images above are just a fraction of the whole image which is actually longer in the vertical direction, we show only a fraction for visual purposes. As we did not take skyflats, some telluric lines are visible even in the reduced spectrum but this can be solved doing a correct calibration and carefully examining the extraction of the spectra of the stars.

3.4.2 Extraction

Once the reduction is ready, we can proceed with the extraction of the spectra of the calibration stars and also the spectra of the stars in the clusters, this procedure is made with the task *apall*. First, I did the extraction of the two calibration stars for each night of observation. For May 14th our calibration stars were HR4963 and HR4468 and for May 15th our calibration stars were HR4468 and HR7950.

Taking special care of correctly choosing the background, and with the following parameter configuration:

b_number: 100 background: fit weight: variance saturate: 65215 rdnoise: 6 gain: 1

Interactively, one must choose very precisely the background regions to extract the spectrum and do the fitting routines with different orders until the best results are reached, the areas of the background are changed using the commands “b” (for setting the background mode) and “s” (for setting the range). A good choice for the background in the case of the calibration star is relatively easy but in the case of the extraction of the stars in the clusters one must take into account the high noise introduced by the other stars and the background so for every star one must zoom into the window using “w” and “a” between the boundaries of the range to be zoomed.

If a good choice of the background and the dispersion axis is well fitted, the task runs straightforward to get the spectrum of the star. In the case of the calibration lamps, the procedure is quite similar because the extraction of their spectrum is done with *apsum*, which is very similar to *apall*.

For the calibration star HR4468, the extracted spectrum looks like the one shown in figure 3.15.

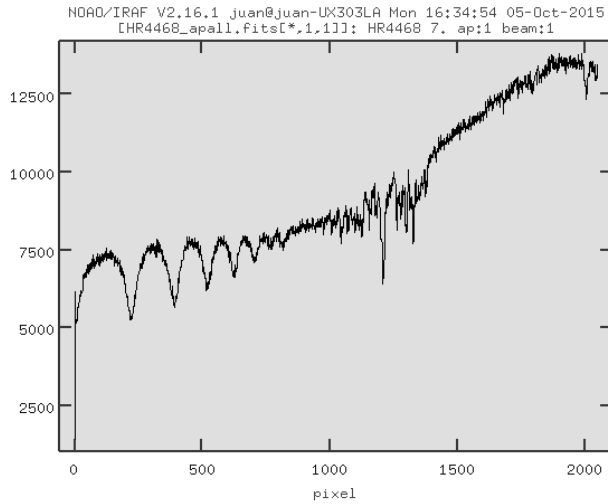


FIGURE 3.15: Extracted spectrum of HR4468, note that the dispersion axis is still in terms of pixels instead of Angstroms, this is fixed by doing the wavelength calibration, also the direction will be shifted because the strong sodium absorption lines are in the left end of the spectrum and they should be in the right end

3.4.3 Wavelength Calibration

Once the spectrum is extracted, the following step is to calibrate it in wavelength in order to make it useful for scientific analysis. The wavelength calibration is made with the use of many tasks of IRAF like *Identify*, *Repspec* and *Dispcor*. First, with *identify* I use the interactive window in IRAF to select some prominent lines in the spectrum

of the calibration lamps and assign them their correct wavelength using the theoretic spectrum of the lamp. In this case our calibration lamps were Ne-Ar (for May 14th) and He-Ar (for May 15th) and OPD observatory provided us the theoretic distribution of emission lines of them. The lines look like the ones shown in figures 3.16 and 3.17

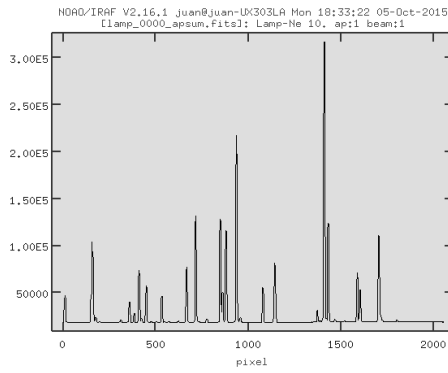


FIGURE 3.16: Emission lines of the Ne-Ar calibration lamp that need to be wavelength calibrated ,the horizontal axis is in pixels and needs to be calibrated to units of wavelength

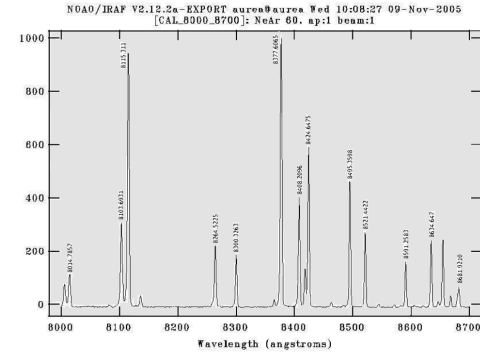


FIGURE 3.17: The theoretic emission lines of the Ne-Ar lamp provided by OPD that we use to make the wavelength calibration, note that the lines to be matched are going in the opposite direction

Running *identify* in the interactive mode and using “m” to select the larger lines and typing the wavelength, the task creates a file stored in a new folder “database” with the pixels with their corresponding values in units of Angstroms. After that, the targets (Calibration Stars and Globular Clusters) need to be calibrated with these files so it is necessary to edit their header to assign them the reference frames. It is enough to change the REFSPEC1 image key header on each lamp file in order to set the wavelength calibration.

The task that actually does the calibration on wavelength for the science targets is *dispcor*, it is only necessary to run the task over all the targets with their own wavelength calibrated lamp to get the calibrated spectrum which is the useful and important file to make the analysis of the width of the lines and their redshift.

The wavelength calibrated spectrum of the star HR4468, after running *dispcor* is show in figure 3.18.

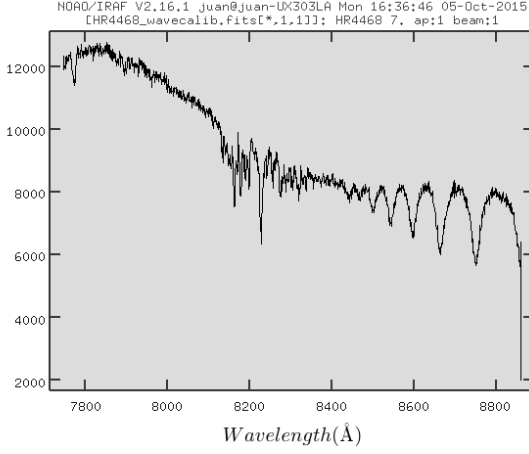


FIGURE 3.18: The spectrum has been wavelength calibrated as we can see in the horizontal axis which is in units of Angstroms. Note that the strong absorption lines are now in the right part of the spectrum, this is because in the process of making the wavelength calibration, the direction of the axis was changed.

In order to see if the wavelength calibration (using the lamps spectra) was correct we used another technique consisting of using a sky spectrum (with no stars or contaminating objects) and identifying some of the atmospheric lines on it, the calibration of the science data is then made with the identified lines in this spectrum. This should be an accurate procedure since the spectrum of the sky is taken exactly with the same instrument and configuration than the science objects and it contains the same atmospheric lines that the GCs spectra.

A secure way to extract the spectrum of the sky was using the original spectrum of a calibration star (reduced *HR4468* in this case) and putting the aperture in an empty region in the image that does not contain any stellar absorption or emission lines. Of course the lines in the extracted spectrum are hard to identify so that the best way to do so is by looking at the already wavelength calibrated spectra of the star (calibrated with the comparison lamps) and identifying its prominent lines, then those lines had to be searched in the web to see how prominent they could be in the atmosphere and what their corresponding wavelength is. Once the information about the prominent emission lines is ready, one can identify them with the task *identify* doing a careful zoom with “w” and “e” in the sky spectrum.

The same procedure consisting on saving a database file with the emission lines and changing the header of the image to calibrate needs to be done in order to complete the calibration.

We used this procedure to calibrate in wavelength *HR4468* and see if both methods gave different results. The relevance of this procedure is that it allows us to see if we have

any systematic problems or errors in the calibrations that would then affect our science data.

After the wavelength calibration was made for the stellar spectrum, we note a difference of around 0.65\AA as we can see in figures 3.19 and 3.20.

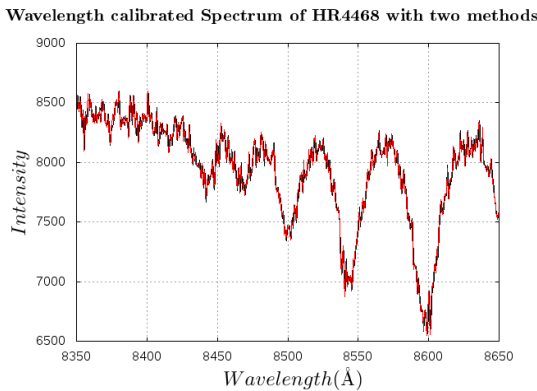


FIGURE 3.19: Comparison between the two wavelength calibration methods. The black line is the spectrum of HR4468 calibrated with the lamp spectra and the red line is the same spectrum calibrated with the sky spectrum

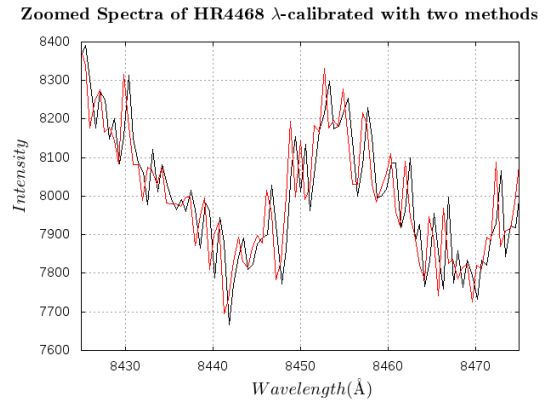


FIGURE 3.20: The same comparison zoomed in a small region to see the shift of the red and black lines. The difference is about 0.65\AA in this region which could mean a difference of about 20km/s in the measured velocities for both spectra.

What this shows is that the radial velocities that we compute may have a small systematic depending on the method we use for the wavelength calibration since even a small shift on the lines would be equal to a difference in velocities of tenths of kilometres per second, thus introducing a big systematic error in our data that would completely affect our modelling. The error bar in the velocities associated with the position of the lines of the spectrum is then too big to give us reliable information about the velocity dispersion in the inner region of the clusters so the calibrations have to be improved.

We needed to find a better solution for this problem because the projected radial velocities are the most important data for our modelling, so we searched for reliable databases that we shall introduce in the “Databases” section at the end of this chapter.

3.4.4 Flux Calibration

This final part of the extraction and calibrations has the aim of calibrating the CCD chip response, spectrograph+telescope throughput and allow for atmospheric extinction. The result is a spectrum as observed from outside the atmosphere with an ideal uniformly sensitive detector+telescope+spectrograph. Basically, what the flux calibration does is, it takes from a tabular compilation the energy distribution of the standard star, it

corrects this energy distribution for wavelength-dependent atmospheric extinction, it compares it to the energy distribution of the observed spectrum and derives from such a comparison the function that gives the response of our system for every wavelength.

The flux calibration takes place in three parts: Calibrating from the standard star, calculating the sensitivity function of the instrument, and finally, applying the calibration to the spectra. We will use the task *observatory* to determine observatory parameters, *standard* to flux calibrate each standard star, and *sensfunc* to finally determine the wavelength response and the solution will be applied to the spectra by the task *calibrate*.

In the first part, the calibration is made with one of the stars that are already included in IRAF, there are many stars so there's quite a good amount of options to choose. So the first task is the task *standard*. The observatory parameter is specified as LNA (Laboratório Nacional de Astrofísica) which is in IRAF's database.

The task standard

The task *standard* determines calibration pass-bands and writes them to a file called "std". The trick here is to specify the location of the the input extinction and flux calibration files. To do that, I edit the parameters of *standard* with the following routes:

Extinction file: onedstds\$/ctioextindt.dat

Directory containing calibration data: onedstds\$ctionewcal/

Starname in calibration list: l9239

Where I chose the Star l9239 because it has the spectral range that we use in our calibration Stars. And running the task interactively would be enough for this step.

The task sensfunc

The task *standard* just recorded response of each standard star so the next step is to put the results together and find a proper wavelength dependence of instrumental sensitivity and atmosphere transparency using the task *sensfunc*. It creates an image with a default name sens.0001. IRAF needs to have some general idea of atmospheric extinction before to start, so I set again extinct onedstds\$ /ctioextinct.dat.

Now, running the task interactively and taking into account that the function used to fit the instrumental response will be usually of very high order. A good idea is to use spline3 fitting (:function spline3) with some 20 pieces, i.e. (:order 20). Finally "q" exists the *sensfunc* task and writes the sens.0001 image.

The task calibrate

The solution to each star to be calibrated is done with the task *calibrate*. Editing the parameters of *calibrate* to set the appropriate extinction table: *extinct onedstds\$ /c-tioextinct.dat* would be enough for this purpose. The task is run over all the wavelength calibrated spectra which had their airmass and other parameters appropriately set by the *eso.set* procedure. And finally it gives the flux-calibrated spectra ready for the relevant analysis concerning radial velocities.

After the flux calibration, I notice that the extremes of the spectra have irregularities given by the flux calibration procedures, but that can be cut because they don't have any relevant information. For the star calibration I create a new copy from pixel 45 to 1860, and the same y-range than the original image using *imcopy*:

```
imcopy flux_calib_star.fits[45:1860,*] cut_flux_calib_star.fits
```

The wavelength and flux calibrated spectrum of the star HR4468, now ready to be used for radial velocities determination is displayed in figure 3.21.

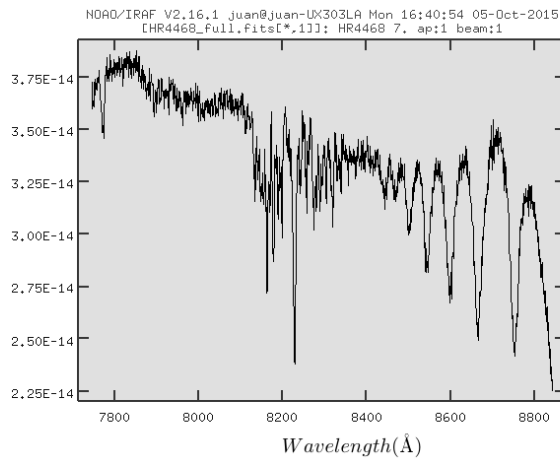


FIGURE 3.21: Flux calibrated spectrum of HR4468 calibration star

In order to normalize the spectrum, first I find the maximum value in the spectrum using *minmax* and then I divide the whole image by this value.

Something that can be very useful is to have the data of the spectrum in a different format so that its information can be well used and analysed with simple programs like *gnuplot*, for this purpose, it is useful to create an Ascii table from the spectrum. For this purpose I need to first convert my image to a 1D image using the task *scopy* and setting *format=onedspec* (this is only necessary if the spectrum was extracted in 2-D).

Now, with the image ready in 1-D, I use the task *wspectext* to create the Ascii table like this:

```
wspectext ready.flux_star.0001.fits normal_cut_flux_star_calib.txt
```

In principle, the same procedures hold for the star in the Globular Clusters, even though it must be made more carefully because the background noise and the crowded space surrounding them affects the spectra and it might change the values of the radial velocities, an example of a wavelength and flux calibrated spectrum of one of the stars in the NGC5139 cluster is shown in figure 3.22.

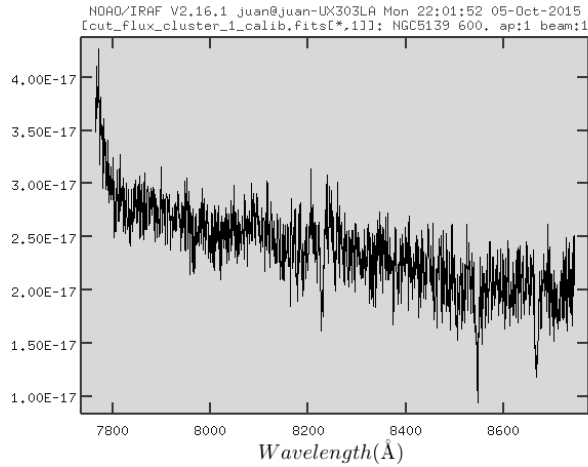


FIGURE 3.22: Spectrum of one of the most prominent stars in the NGC5139 cluster, after all the calibrations have been made

Although the noise is evidently higher than in the case of the spectrum of the calibration star, it is possible to see (even with the naked eye) two of the calcium strong absorption lines around 8543Å and 8663Å. After all of these procedures have been made to the important stars in the clusters and the calibration stars, the next step is to explore the best way to determine radial velocities with the use of some sophisticated tasks in IRAF such as *RVS*AO, as we discuss in the next section.

3.5 Radial velocity determination

In order to study the dynamics of the starts within the stellar systems we used various techniques with the spectroscopic data. One consists of extracting the spectrum of each individual star and measuring the shifting of the lines (with respect to the rest frame) to measure its radial velocity so that we can obtain the projected velocity dispersion; another technique consists of using the full integrated spectrum of each cluster and measure the Doppler broadening of the lines (as shown in Figure 2.9) to directly get information about the velocity dispersion with respect to a rest frame template.

Our radial velocity determination started with the first technique (analysing spectra of individual stars) with the IRAF package RVSAO:

3.5.1 RVSAO

This package is the radial velocity analysis package of the Smithsonian Astrophysical Observatory and is intended to properly organize a set of programs to obtain redshifts and radial velocities from spectra. It contains (by 2015) 26 programs well documented for the users' need. We focus on the task XCSAO as well as the utilities of EMSAO and BCVCOR for our set of data.

The program XCSAO is the most important one in the RVSAO package, it implements the cross-correlation method and interactive algorithms to properly prepare the spectra for a correct radial velocity analysis such as the removal of the continuum and the emission line suppression. For using this task, one must provide the spectrum of the object and a template spectrum (preferably in the rest frame so that the emission and absorption lines are in their proper wavelength) that will be used for the cross correlation, it also requires the starting and ending wavelength, the type of Fourier filtering and many other details according to the user's desires and interests.

By using one of IRAF's templates “*habtemp0.fits*” that covers the range of 2884.1547Å to 7037.3375Å we can directly run XCSAO on a stellar spectrum that will use the Fourier transform to cross correlate them and give an approximate value of the radial velocity of the star and printed in an irafterm window as seen in figure 3.23.

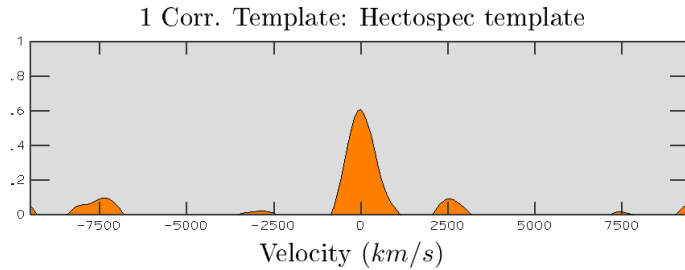


FIGURE 3.23: The relevant part of XCSAO results, the cross correlation in this case is good and shows a well-behaved peak, the radial velocity of the star in this case is around -30 km/s

The results of RVSAO have a really strong dependence on the quality of the template used for the cross correlation, and some of the IRAF spectra have different wavelength ranges and flux values on the characteristic lines so that they won't give reliable results. One is forced to create a template spectrum with the most prominent lines to be used to correlate the object spectrum. One task that can be very useful in the creation of the templates is *rspectext* that creates an image spectrum from an ascii table where the

user can set the dispersion to be assigned to the spectra, and the appropriate values for the flux and intensity of absorption or emission lines.

One of our created templates that holds information about some absorption lines including the calcium triplet and made using *rspectext* is shown in figure 3.23.

| Wavelength | Intensity | Line |
|------------|-----------|------|
| 8497.84 | -0.8 | CaII |
| 8542.09 | -0.89 | CaII |
| 8598.49 | -0.872 | HI |
| 8661.74 | -1.0 | CaII |
| 8750.91 | -0.97 | HI |

TABLE 3.2: Input data for the creation of template with *rspectext*. The user specifies the value of the wavelength λ (Column 1), the approximate intensity of the lines (Column 2) and the name of the spectral feature (Column 3).

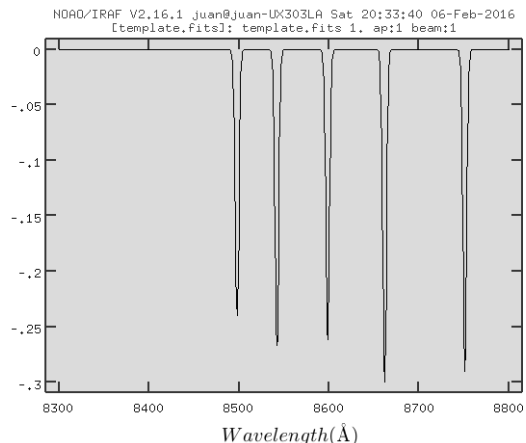


FIGURE 3.24: Results of the template spectrum created by *rspectext* in the given wavelength range with the values of table 3.2, this template does not have any emission lines since our spectra didn't have strong emission features.

Another important issue to be addressed when we analyse radial velocities is the fact that our ground based observations are done in a moving system around the Sun and around the galaxy so that the Doppler shift of the lines would be affected by this relative movement of the Earth with respect to the Sun's velocity that the Earth is attached to. The issue can be seen in the following figure.

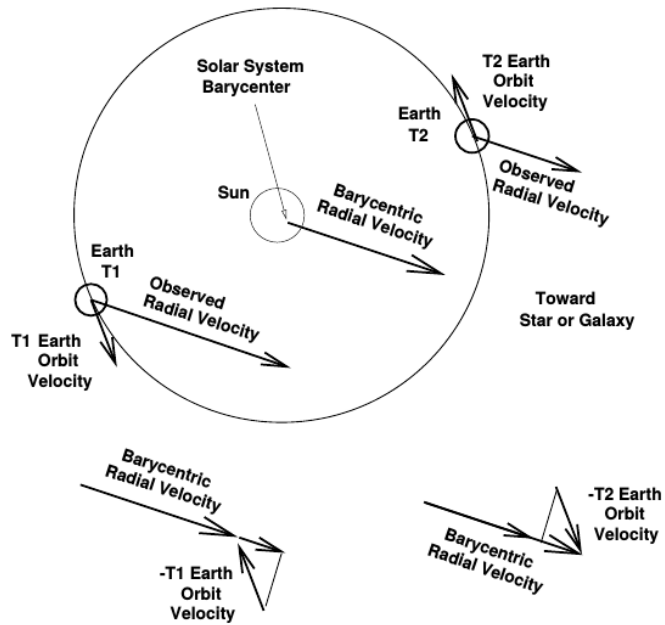


FIGURE 3.25: Correction of radial velocity observed from the earth to the radial velocity observed from the center of mass of the solar system shown at two different times in the earth's orbit, M. Kurtz, D. Mink 1993 [1]

The barycenter correction of the spectra can be made using the task BCVCOR, the task calculates the correction of the barycenter velocity according to the date of the observation and edits the header of the image so that this information will be stored and read by other tasks like XCSAO by the time the radial velocity calculation is to be made. Another important task of the RVSAO package is EMSAO that computes redshifts by identifying shifted emission lines in the spectrum with respect to templates with emission lines in the rest frame. This task might be very useful if the spectra has strong emission features but the cross correlation techniques used by XCSAO might give a better choice if the spectrum has important absorption lines. As seen in the following figure, EMSAO identifies the strong features of the spectrum to be measured using files in the IRAF database that contain information about emission lines with their given wavelength:

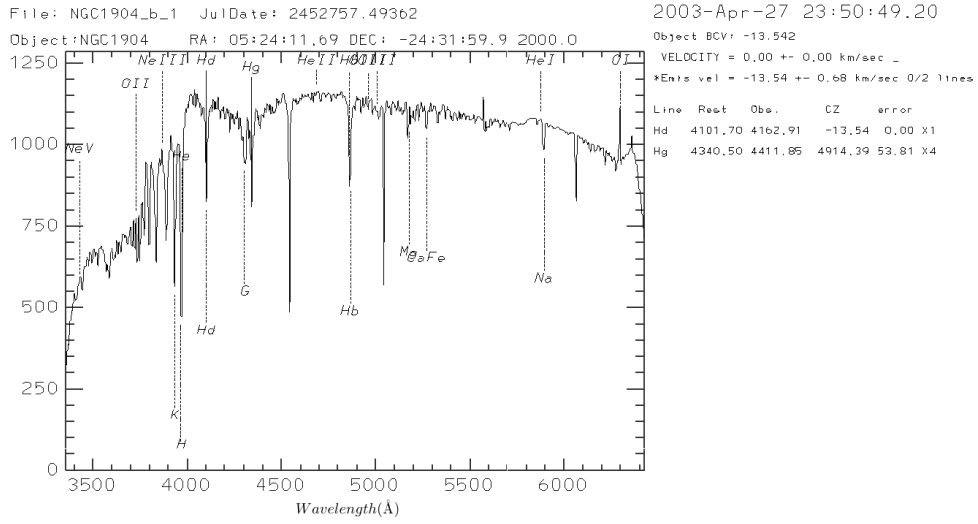


FIGURE 3.26: EMSAO results with the identification of strong absorption lines in the integrated spectrum of the Globular Cluster NGC1904 but few emission, note that the spectrum has already a barycentric velocity correction (BCV) of -13 km/s , specified in the header as explained before.

One of the other techniques we used to study velocity dispersions in GCs spectra was using another IRAF task that also uses cross correlation techniques like XCSAO but runs much more straightforward and has a strong advantage regarding the output information after the fitting is made, the task is FXCOR.

3.5.2 FXCOR

This IRAF package, very useful for radial determination decomposes every signal in a sum of sinusoidal functions through the Fourier transformation of a spectrum that has been wavelength calibrated. The product of the transformed signals generates the correlation function, which is similar to a Gaussian function and displayed in the irafterm after the task has been run. The stronger the correlation is, the higher the peak of the curve is, to a maximum of 1 (for the perfect correlation) in the case of an autocorrelation. Regarding the results of the correlation, the peak height is index of the superposing grade of the two spectra because it depends on the presence of the same absorption (or emission) lines as explained by V. Guglielmo et al. 2009 [16].

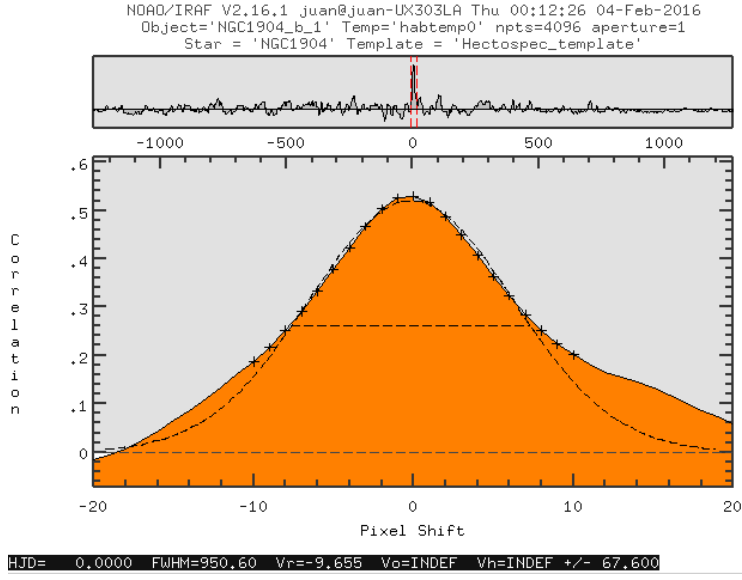


FIGURE 3.27: FXCOR cross correlation results for NGC1904 with the IRAF template habtemp0 with a measured radial velocity of -9.655 km/s , note that the peak has a well-behaved shape and it is the strongest peak so that the correlation gave good results.

Besides the radial velocity calculation made by this task, for our purposes its most important feature is the fact that it also measures the width of the peak at the middle height (FWHM), which is useful to calculate the velocity dispersion of integrated spectra with the following relations:

The first thing we have to do is calculate the intrinsic FWHM_i , which is in terms of the FWHM of the correlation and the FWHM of the autocorrelation of the object spectrum (FWHM_a):

$$\text{FWHM}_i = \sqrt{\text{FWHM}^2 - \text{FWHM}_a^2} \quad (3.1)$$

With the intrinsic FWHM_i , the velocity dispersion given by the object spectrum is given by:

$$\sigma = \frac{\text{FWHM}_i}{2.35} \quad (3.2)$$

And thus, using the virial theorem to relate the kinetic to the potential energy one can calculate the mass of the object (GCs in our case) is given by:

$$M = \frac{r_e \sigma^2}{0.33G} \quad (3.3)$$

With r_e the half mass radius (where half of the galaxy light is contained)

Our radial velocity determination involves the necessity of creating or finding very accurate templates because as it has been mentioned, the results of the correlation are highly dependent on the quality of the absorption and emission lines in them.

3.6 Databases

Besides our observational data we decided to use different published databases from all over the world in order to do our modelling. We searched for high quality and well-reported data that gave us good confidence upon our results.

In the first part of our modelling, we focus on the radial profile of the projected velocity dispersion so we needed radial velocities of stars in the cluster. The radial-velocity databases that we decided to use (after filtering out repeated or low quality data) are organized in table 3.3.

| Article | Bibcode | Description |
|----------------------|----------------------|---------------------------------------|
| Da Costa et al. 2008 | 2008AJ....136..506D | 1355 stars. ~ 204 cluster stars |
| Johnson et al. 2008 | 2008ApJ...681.1505J | 180 cluster stars |
| Mayor et al. 1997 | 1997AJ....114.1087M | 481 stars. ~ 381 cluster stars |
| Pancino et al. 2007 | 2007ApJ...661L.155P | 649 cluster stars |
| Sollima et al. 2009 | 2009MNRAS.396.2183S | 946 stars (Including Pancino's data) |
| Reijns et al. 2006 | 2006A& A...445..503R | 1966 stars. ~ 1592 cluster stars |

TABLE 3.3: Reported values of Omega Centauri's radial velocities, each of the databases included their measured error and were J2000 Julian date.

As further reference, we searched for reported values of the dynamical mass of ω Centauri, in table 3.4

| Article | Mass (M_{\odot}) |
|--------------------------|----------------------|
| Mandushev et al. 1991 | 2.4×10^6 |
| Pryor & Meylan | 3.98×10^6 |
| Meylan et al. 1995 | 5.1×10^6 |
| Majewski et al. 2000 | 5.1×10^6 |
| Van de Ven et al. 2006 | 2.5×10^6 |
| Cassini et al. 2009 | 3.0×10^6 |
| Valcarce & Catelan, 2011 | 3.0×10^6 |
| Jalali et al. 2011 | 2.5×10^6 |

TABLE 3.4: Reported values of Omega Centauri's dynamical mass

Chapter 4

Modelling

We used various techniques for the mass modelling of ω Centauri, so that we could make a good approximation to its dynamic and stellar mass. In order to do this, we decided to use the Hernquist profile and made some modifications on it so that dark matter contributions would also be included.

4.1 Modified Hernquist Model

Our modelling is based on significant modifications to the Hernquist profile (Hernquist 1989). We use this model because it is a well known model that closely approximates the de Vaucouleurs law for elliptical galaxies and has analytical solutions that can be useful for our computational purposes. As introduced in chapter 2, the density profile for this model is

$$\rho(r) = \frac{M}{2\pi r} \frac{1}{(r+a)^3} \quad (4.1)$$

It's associated cumulative mass is

$$M(r) = M \frac{r^2}{(r+a)^2} \quad (4.2)$$

And the surface brightness

$$I(R) = \frac{M}{2\pi a^2 \Gamma(1-s^2)^2} [(2+s^2) X(s) - 3] \quad (4.3)$$

where $s = R/a$, R is the projected radius and:

$$X(s) = \frac{1}{\sqrt{1-s^2}} \operatorname{sech}^{-1} s \quad \text{for } 0 \leq s \leq 1 \quad (4.4)$$

$$X(s) = \frac{1}{\sqrt{s^2-1}} \operatorname{sec}^{-1} s \quad \text{for } 1 \leq s < \infty \quad (4.5)$$

For computational simplicity we have written some of the trigonometric functions just like Hernquist did: $\operatorname{sec}^{-1} s = \cos^{-1}(1/s)$ and $\operatorname{sech}^{-1} = \ln[(1+\sqrt{1-s^2})/s]$. As mentioned in the theoretical framework chapter, the line of sight velocity dispersion in the more general case with the anisotropy parameter different from 0 we have

$$I(R)\sigma_p^2(R) = \frac{2}{\Gamma} \int_R^\infty \left(1 - \beta \frac{R^2}{r^2}\right) \frac{\rho \bar{v}_r^2 r dr}{\sqrt{r^2 - R^2}} \quad (4.6)$$

And the radial velocity dispersion (introduced in chapter 2), in terms of the potential and the density is

$$\bar{v}_r^2 = \sigma_r^2 = \frac{1}{\rho(r)} \int_r^\infty \rho(r) \frac{d\phi}{dr} dr \quad (4.7)$$

Where

$$\frac{d\phi}{dr} = \frac{GM(r)}{r^2} \quad (4.8)$$

So the projected velocity dispersion becomes:

$$\sigma_p^2(R) = \frac{2}{I(R)\Gamma} \int_R^\infty \left(1 - \beta \frac{R^2}{r^2}\right) \left(G \int_r^\infty \frac{\rho(r)M(r)}{r^2} dr\right) \frac{r dr}{\sqrt{r^2 - R^2}} \quad (4.9)$$

We do various experiments for our modelling, the simplest of all models is the one where we assume that the cluster doesn't have dark matter whatsoever, in this case there only will be one mass contribution and only one scalength (the stellar scalength) so the solution of the last equation would be:

$$\sigma_p^2(R) = \frac{GM^2 a}{I(R)\Gamma\pi} \int_R^\infty \alpha(r) \left(\frac{\log\left(\frac{a+r}{r}\right)}{a^5} - \frac{25a^3 + 52a^2r + 42ar^2 + 12r^3}{12a^4(a+r)^4} \right) dr \quad (4.10)$$

Where a is the scalength and where, in order to shorten the equation we take $\alpha(r)$ as

$$\alpha(r) = \left(1 - \beta \frac{R^2}{r^2}\right) \frac{r}{\sqrt{r^2 - R^2}} \quad (4.11)$$

Now, as we want to focus on the dark matter content of the cluster, we assume that the mass of the cluster is the sum of the mass of stars and the mass of non-baryonic matter so that their contributions to the density and mass profiles become:

$$\rho(r) = \rho_s(r) + \rho_{dm}(r) \quad \text{and} \quad M(r) = M_s(r) + M_{dm}(r) \quad (4.12)$$

In this case, the projected velocity dispersion takes a much more complicated form as follows:

$$\begin{aligned} \sigma_p^2(R) &= \frac{G}{I(R)\Gamma\pi} \int_R^\infty \alpha(r) \left[\underbrace{\int_r^\infty \frac{M_s^2 a_s dr}{r(r+a_s)^5}}_{\mathbf{A}(r)} + \underbrace{\int_r^\infty \frac{M_s M_{dm} a_s dr}{r(r+a_s)^3 (r+a_{dm})^2}}_{\mathbf{B}(r)} \right. \\ &\quad \left. + \underbrace{\int_r^\infty \frac{M_{dm} M_s a_{dm} dr}{r(r+a_{dm})^3 (r+a_s)^2}}_{\mathbf{C}(r)} + \underbrace{\int_r^\infty \frac{M_{dm}^2 a_{dm} dr}{r(r+a_{dm})^5}}_{\mathbf{D}(r)} \right] dr \end{aligned} \quad (4.13)$$

The functional form of the density involves the use of a stellar scalength (a_s) and a dark matter scalength (a_{dm}). Now, the integrals $\mathbf{A}(r)$, $\mathbf{B}(r)$, $\mathbf{C}(r)$ and $\mathbf{D}(r)$ have the following analytical solutions:

$$\mathbf{A}(r) = a_s \left(-\frac{25a_s^3 + 52a_s^2 r + 42a_s r^2 + 12r^3}{12a_s^4 (a_s + r)^4} + \frac{\log \left[\frac{a_s+r}{r} \right]}{a_s^5} \right) \quad (4.14)$$

$$\mathbf{D}(r) = a_{dm} \left(-\frac{25a_{dm}^3 + 52a_{dm}^2 r + 42a_{dm} r^2 + 12r^3}{12a_{dm}^4 (a_{dm} + r)^4} + \frac{\log \left[\frac{a_{dm}+r}{r} \right]}{a_{dm}^5} \right) \quad (4.15)$$

$$\mathbf{B}(r) = \frac{(M_s M_{dm}) (\mathbf{b}_2 + \mathbf{b}_3 + a_s (- (a_s - a_{dm}) a_{dm} \mathbf{b}_4 + \mathbf{b}_5))}{\mathbf{b}_1} \quad (4.16)$$

$$\text{With } \left\{ \begin{array}{l} \mathbf{b}_1 = 2a_s^2(a_s - a_{dm})^4 a_{dm}^2 (a_s + r)^2 (a_{dm} + r) \\ \mathbf{b}_2 = -2(a_s - a_{dm})^4 (a_s + r)^2 (a_{dm} + r) \log r \\ \mathbf{b}_3 = 2a_{dm}^2 (6a_s^2 - 4a_s a_{dm} + a_{dm}^2) (a_s + r)^2 (a_{dm} + r) \log [a_s + r] \\ \mathbf{b}_4 = 2a_s^4 + 4a_s^3 r - 2a_{dm} r (a_{dm} + r) + 3a_s a_{dm} (-a_{dm}^2 + a_{dm} r + 2r^2) \\ \quad + a_s^2 (7a_{dm}^2 + 7a_{dm} r + 2r^2) \\ \mathbf{b}_5 = 2a_s^2 (a_s - 4a_{dm}) (a_s + r)^2 (a_{dm} + r) \log [a_{dm} + r] \end{array} \right. \quad (4.17)$$

$$\mathbf{C}(r) = \frac{(M_{dm} M_s) (\mathbf{c}_2 + \mathbf{c}_3 + a_{dm} (-(a_{dm} - a_s) a_s \mathbf{c}_4 + \mathbf{c}_5))}{\mathbf{c}_1} \quad (4.18)$$

$$\text{With } \left\{ \begin{array}{l} \mathbf{c}_1 = 2a_{dm}^2 (a_{dm} - a_s)^4 a_s^2 (a_{dm} + r)^2 (a_s + r) \\ \mathbf{c}_2 = -2(a_{dm} - a_s)^4 (a_{dm} + r)^2 (a_s + r) \log r \\ \mathbf{c}_3 = 2a_s^2 (6a_{dm}^2 - 4a_{dm} a_s + a_s^2) (a_{dm} + r)^2 (a_s + r) \log [a_{dm} + r] \\ \mathbf{c}_4 = 2a_{dm}^4 + 4a_{dm}^3 r - 2a_s r (a_s + r) + 3a_{dm} a_s (-a_s^2 + a_s r + 2r^2) \\ \quad + a_{dm}^2 (7a_s^2 + 7a_s r + 2r^2) \\ \mathbf{c}_5 = 2a_{dm}^2 (a_{dm} - 4a_s) (a_{dm} + r)^2 (a_s + r) \log [a_s + r] \end{array} \right. \quad (4.19)$$

As we mentioned in the last chapter, we used many databases for projected radial velocities in order to properly do our fit and modelling. The data is shown in figure 4.1

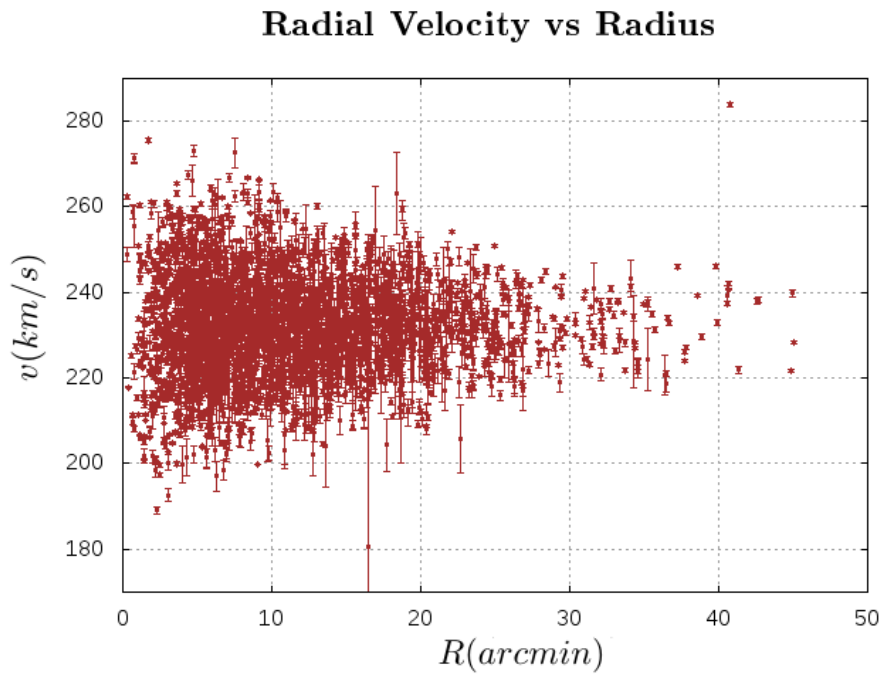


FIGURE 4.1: Pd

Because we need to calculate the projected velocity dispersion profile, we need to cut in radial bins as shown in figure 4.2

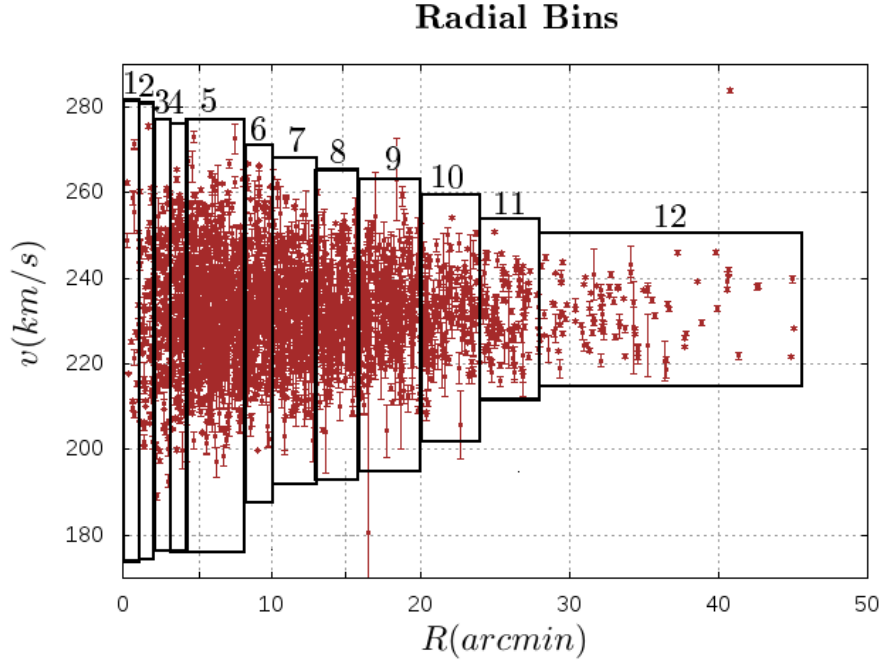


FIGURE 4.2: Pd

The velocity dispersion is the standard deviation of the velocity

$$\sigma = f(v) = \sqrt{\frac{\sum_{i=1}^n (v_i - v)^2}{N}} \quad (4.20)$$

In order to do a proper modelling and fitting we need to take into account the error associated with σ_p . Because all the databases provided the associated error to the measurements of the radial velocities, we made the proper calculation of the error of the velocity dispersion using the general error propagation formula

$$\sigma(v \pm \Delta v) \approx \sigma(v) \pm \underbrace{\frac{\partial \sigma}{\partial v} \Delta v}_{\Delta \sigma} \quad (4.21)$$

$$\Delta \sigma = \frac{1}{\sqrt{N}} \left(\sum_{i=1}^n (v_i - v)^2 \right)^{-1/2} \sum_{i=1}^n (v_i - v) \Delta v \quad (4.22)$$

With the radial projected velocity dispersion (and its error) we can start with the fitting to find the optimized parameters in our various experiments. Because the functions that we wanted to fit did not have an analytic solution, we decided use a χ^2 method instead.

This approximation method allows to fit curves to the observational data so that the parameters would be optimized, that is, the combination of parameters would allow the curve to fit well the observational data. Our programs written in C were set so that the χ^2 was calculated for every combination of the parameters (every entry of the parameters matrix) but it will only save the values of the parameters that make the smallest χ^2 . If we call $\sigma_M(r_i)$ the value of our modelling for the radial bin i and if σ_i is the observational value of the projected velocity dispersion in the same bin, we show that our calculation of this approximation method is given by

$$\chi^2 = \sum_{i=1}^n \frac{1}{N_i} (\sigma_M(r_i) - \sigma_i)^2 \quad (4.23)$$

Where N_i is the number of velocities used to calculate the velocity dispersion in bin i (this was included to give more weight to the radial bins that were calculated with a higher number of data), and n is the number of radial bins. By doing these runs over big Δs and then refining them, we obtain the following results for each of our experiments.

4.1.1 Full Modelling

This first set of experiments consisted of the variation of every parameter of our modelling, that is, dark matter mass M_{dm} , stellar mass M_s , dark matter scalength a_{dm} , stellar scalength a_s , mass-to-light ratio Γ and parameter of anisotropy β .

Because some authors (Jalali et al. 2012) state that there might be a medium-mass black hole at the center of ω Centauri, we decided to conduct two different fittings, one with the central region of the cluster (12 radial bins) and other without the central region of the cluster (10 radial bins), and in each group of experiments we made four basic assumptions to take into account all the possibilities of our modelling:

- i)* We don't use the crossed terms in equation 4.13, because we wanted to see how relevant they were in the modelling, we call this “*No crossed terms*”.
- ii)* We assume a constant stellar scalength taken from the literature, we call this “*Fix a_s* ”.
- iii)* We don't assume any of our parameters to be constant, we call this “*full modelling*”.
- iv)* We assume the cluster doesn't have any dark matter so the solution of the equation 4.9 is much simpler and it's given by 4.10, we call this “*No Dark matter*”.

Now, let's see the results for all of these experiments with the graphs that show the fitting and the optimized values of the parameters found for the minimum χ^2

Full fits with 12 radial bins

We figure 4.3

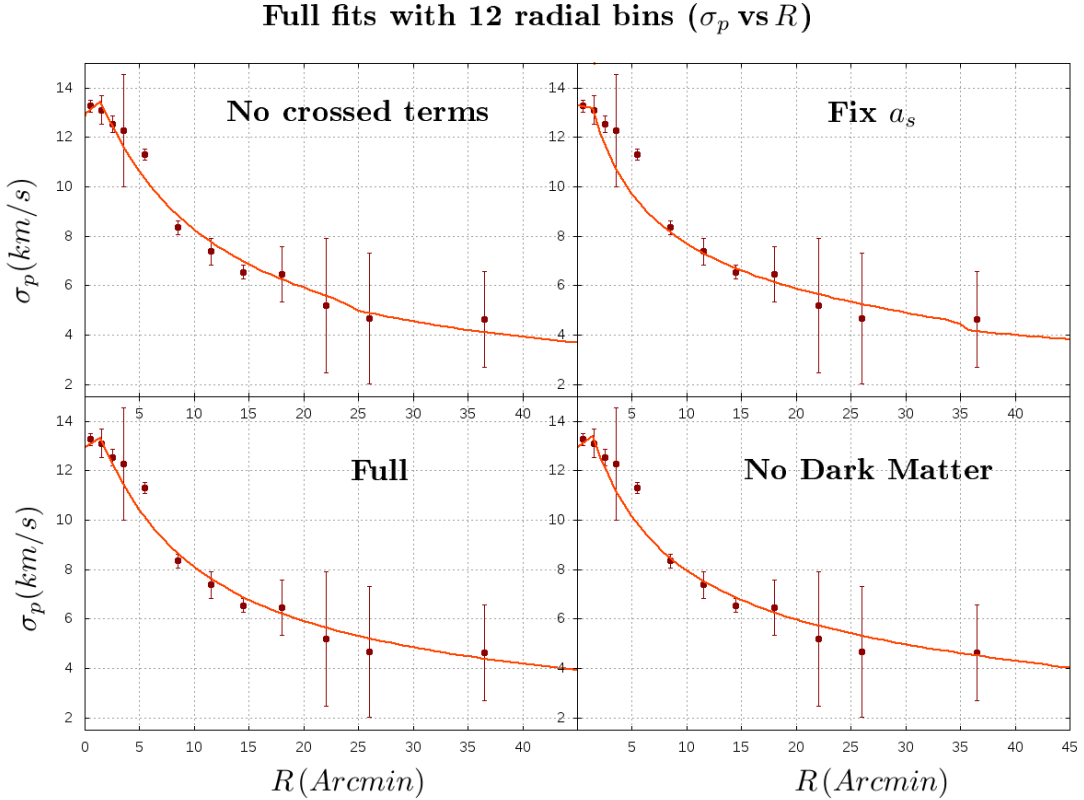


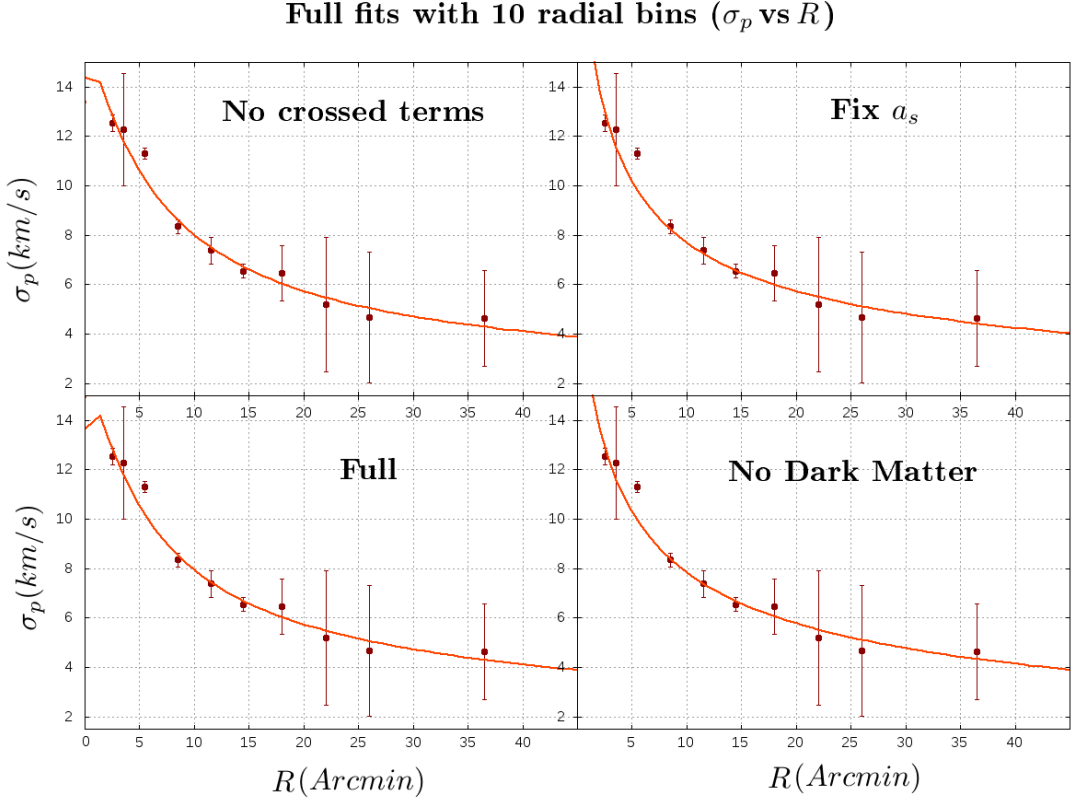
FIGURE 4.3: Pd

| Experiment | β | $a_{\text{dm}}(pc)$ | $a_s(pc)$ | $M_{\text{dm}}(M_\odot)$ | $M_s(M_\odot)$ | Γ |
|------------------|---------|---------------------|------------|--------------------------|------------------------|----------|
| No Crossed terms | 0.62 | 15.8 | 29.0 | 5.6×10^5 | 8.0×10^4 | 2.2 |
| Fix a_s | 0.0001 | 9.0 | 2.23 | 1.12×10^5 | 1.06×10^6 | 1.5 |
| Full | 0.46 | 15.2 | 52.6 | 9×10^5 | 9×10^5 | 0.38 |
| No Dark Matter | 0.26 | \sim | $a = 3.64$ | \sim | $M = 1.98 \times 10^6$ | 1.24 |

TABLE 4.1: Ie

Full fits with 10 radial bins

figure 4.4

**FIGURE 4.4:** Pd

| Experiment | β | $a_{\text{dm}}(pc)$ | $a_s(pc)$ | $M_{\text{dm}}(M_\odot)$ | $M_s(M_\odot)$ | Γ |
|-------------------|---------|---------------------|------------|--------------------------|---------------------|----------|
| No Crossed terms | 0.6 | 16 | 52.8 | 2.1×10^6 | 2.72×10^6 | 2.3 |
| Fix a_s | 0.79 | 57.9 | 2.23 | 8×10^5 | 3.43×10^6 | 2.1 |
| Full | 0.04 | 11.8 | 57.8 | 6×10^5 | 9×10^5 | 2.1 |
| No Dark Matter | 0.78 | \sim | $a = 2.96$ | \sim | $M = 3 \times 10^6$ | 1.94 |

TABLE 4.2: Ie

4.1.2 Fix mass-to-light ratio

In this set of experiments, the mass-to-light ratio Γ is a fix value that we found by fitting the effective radius in a de Vaucouleurs profile on the surface brightness of Eva Noyola's observational data (Noyola et al. 2013) shown in figure 4.5

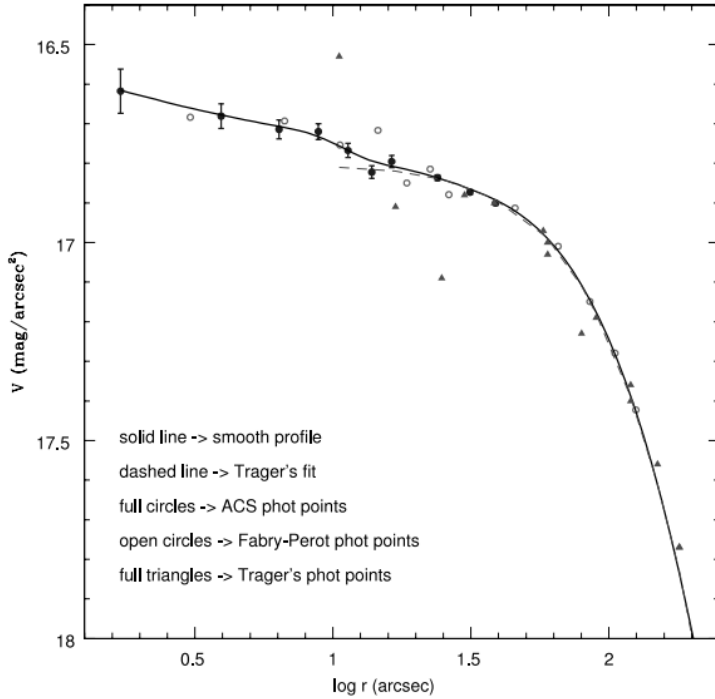


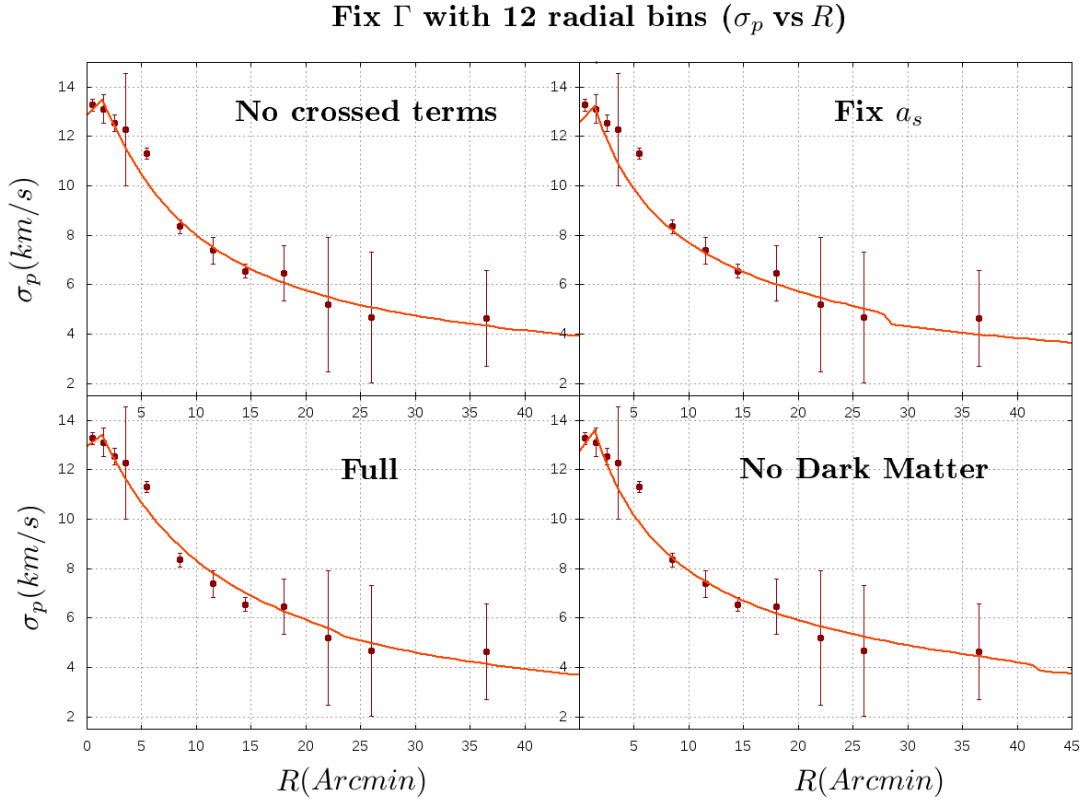
FIGURE 4.5: Surface brightness profile for ω Centauri. The circles show Noyola's measured photometric points. The triangles show photometric points obtained from ground based images by Trager et al. The dashed line is Trager's Chebychev fit. The solid line is Noyola's smooth fit that we don't use for our fitting of the scalength. Figure taken from Noyola et al. 2013

Our fitting (easily made with Mathematica) gives us an effective radius of $R_e = 4.048$ and using the relation $R_e \approx 1.8153a$ (Hernquist 1989), we find a stellar scalength of $a = 2.23$ that we use for our set of experiments. The other parameters (M_{dm} , M_s , a_{dm} , a_s , β) were again varied to find the smallest χ^2 .

Once again, we do our experiments with 10 and 12 radial bins (for the problems that the black hole could do in the fitting) and we take into account the four possibilities discussed above.

Fix mass-to-light ratio with 12 radial bins

figure 4.6

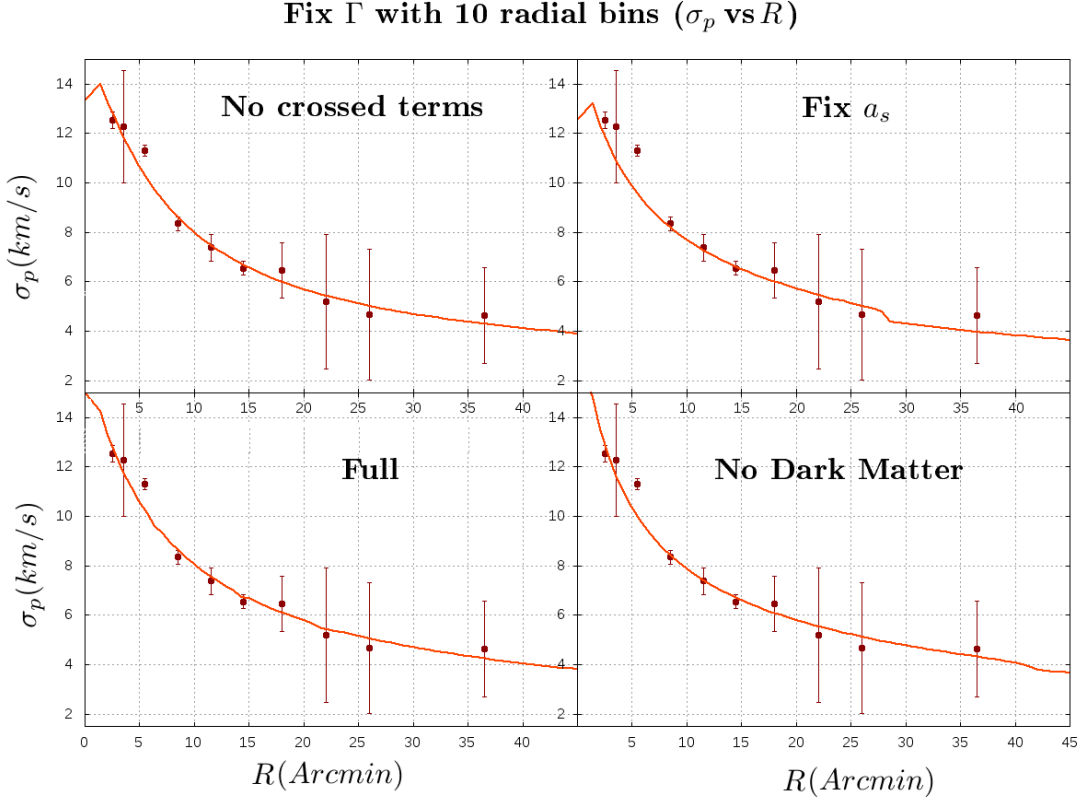
**FIGURE 4.6:** Pd

| Experiment | β | $a_{dm}(pc)$ | $a_s(pc)$ | $M_{dm} (M_\odot)$ | $M_s (M_\odot)$ | Γ |
|------------------|---------|--------------|------------|--------------------|------------------------|----------|
| No Crossed terms | 0.35 | 16.4 | 55.62 | 1.62×10^6 | 2.1×10^6 | 2.5 |
| Fix a_s | 0.001 | 3.0 | 2.23 | 3×10^5 | 5.0×10^5 | 2.5 |
| Full | 0.72 | 20.0 | 44.4 | 5.2×10^5 | 8.0×10^4 | 2.5 |
| No Dark Matter | 0.001 | \sim | $a = 3.15$ | \sim | $M = 1.52 \times 10^6$ | 2.5 |

TABLE 4.3: Ie

Fix mass-to-light ratio with 10 radial bins

figure 4.7

**FIGURE 4.7:** Pd

| Experiment | β | $a_{\text{dm}}(pc)$ | $a_s(pc)$ | $M_{\text{dm}}(M_\odot)$ | $M_s(M_\odot)$ | Γ |
|------------------|---------|---------------------|------------|--------------------------|------------------------|----------|
| No Crossed terms | 0.2 | 15.2 | 59.8 | 1.4×10^6 | 2.1×10^6 | 2.5 |
| Fix a_s | 0.801 | 3.0 | 2.23 | 5×10^5 | 1.0×10^5 | 2.5 |
| Full | 0.9 | 16.0 | 44.6 | 1.62×10^6 | 1.42×10^6 | 2.5 |
| No Dark Matter | 0.38 | \sim | $a = 2.38$ | \sim | $M = 2.03 \times 10^6$ | 2.5 |

TABLE 4.4: Ie

4.2 Stellar Population Synthesis with Starlight

The stellar mass content of Globular Clusters and Galaxies can be studied through the determination of the stellar populations inside those systems since we have clear knowledge about their photometric properties. If we have information about the amount of stars of a given type inside a stellar system, we can infer how much of the system's mass is given by these populations of stars.

The determination of the stellar populations can be done using STARLIGHT, which is a Fortran-based program that fits an observed integrated spectrum (Omega Centauri in

our case) with a model spectrum which is the sum of N_* spectral components from a pre-defined and pre-processed set of base spectra. The program does as many iterations as the user decides to sum up the different template spectra until a good fitting of the spectral lines has been made to the observed spectrum.

The output of the program after the execution contains the created spectrum (wavelength and intensity) and the approximate percentage of each of the stellar population inside the stellar system. Since the stellar populations are well documented the output will also contain the metallicity of each of them so that further analysis can be made upon STARLIGHT's results.

First, one must prepare the observed spectrum before running STARLIGHT, the spectrum has to be wavelength and flux calibrated, taking into account the bad-pixel removal. Very importantly in the context of mass analysis, the spectrum has to be extinction corrected so that the units of flux relate properly to the units if the templates in STARLIGHT.

The extinction correction for our observed spectrum is given by

$$f_{obs}(\lambda) = f_{int}(\lambda)10^{-0.4A_\lambda} \quad (4.24)$$

Where $A_\lambda = 0.213$ in the I filter around 8000Å, around the wavelength range of our spectrum.

On our case, we have to multiply by a factor of 1.216746 the intensity of the spectrum for the flux calibration to be made. After we apply the extinction correction to the spectrum and create an ASCII table with the wavelength, intensity and error columns, it is now ready to be processed with STARLIGHT as we can see in the following figure:

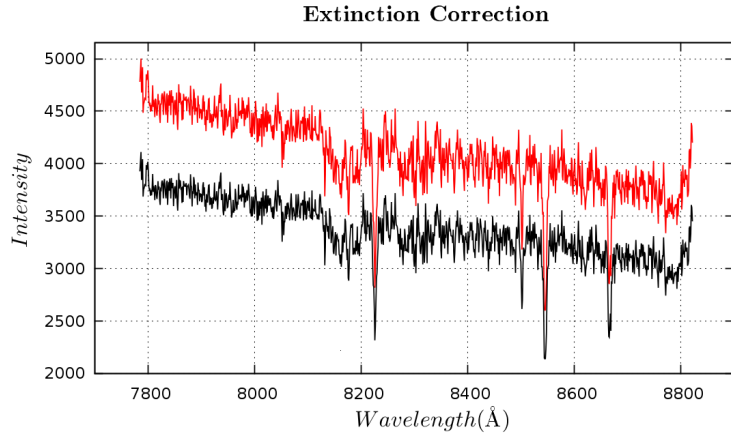


FIGURE 4.8: This figure shows an integrated spectrum of the central region of Omega Centauri before and after the extinction correction is applied. The black line has the original flux values and the black line has the corrected flux, that is, the flux that would be observed if there wasn't any interstellar medium that obscures the light coming from the object.

Before running STARLIGHT one must assure that the wavelength range is correctly specified in the configuration file that also includes the database of the template spectra and the bad data organized in a mask file. When all of these is ready it is straightforward to run STARLIGHT with the following command:

```
./StarlightChains_v04.exe < Omega_cen.in
```

The synthetic spectrum and the original one look like this:

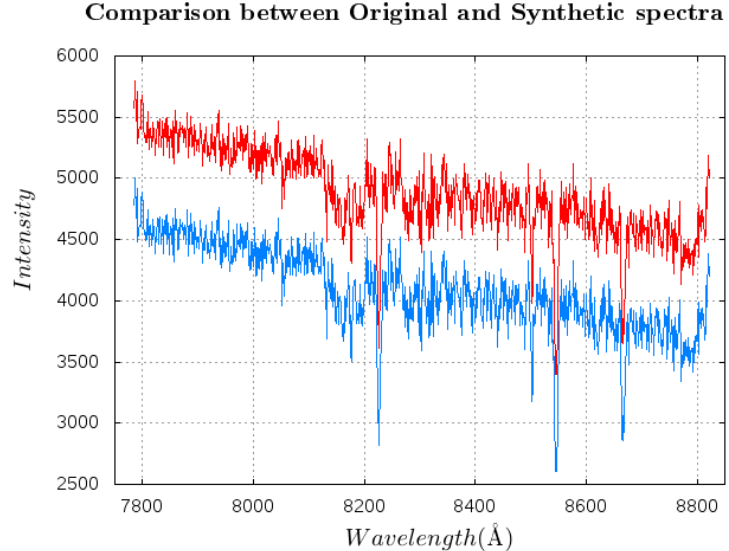


FIGURE 4.9: Synthetic spectrum of Starlight in red, shifted in the y axis for doing the comparison with the original spectrum of Omega Centauri in blue.

Now, besides the synthetic spectrum, the output file contains some useful results that one can use to calculate the mass of the stellar system. In our case, the relevant parameter that STARLIGHT gives is the stellar mass parameter given by:

$$M_{cor_tot} = 3.29446 \times 10^7 \quad (4.25)$$

And using the formula:

$$M_s = M_{cor_tot} \times 10^{-17} \times 4\pi d^2 \times (3.826 \times 10^{33})^{-1} \quad (4.26)$$

Where d is the luminosity distance in cm, yields a stellar mass of $M_\star = 243.462 M_\odot$

This mass is the stellar mass contained in the detection area (that in our set up configuration in OPD ends up to be $A_D = 0.36 pc^2$) of the integrated spectrum that we analysed with STARLIGHT so if we want to calculate the whole stellar mass of the Globular system we must extrapolate this result to its whole effective area, noting that this will increase the error of the calculation.

If we take the cluster's tidal radius of $40'$ and it's distance to the sun of $4808.39 pc$ using a distance modulus of 13.41 , then the total effective area (where the stellar mass could be calculated using stellar population synthesis) is $A_{OC} = 9833.8 pc^2$.

Finally, the total stellar mass of the Cluster using this technique can be calculation using:

$$M_{sT} = N \times M_\star \quad (4.27)$$

Where N is the number of detection areas within the total effective area of Omega Centauri (A_{OC}/A_D) of about 31844.8 . So that our calculation of the stellar mass is finally:

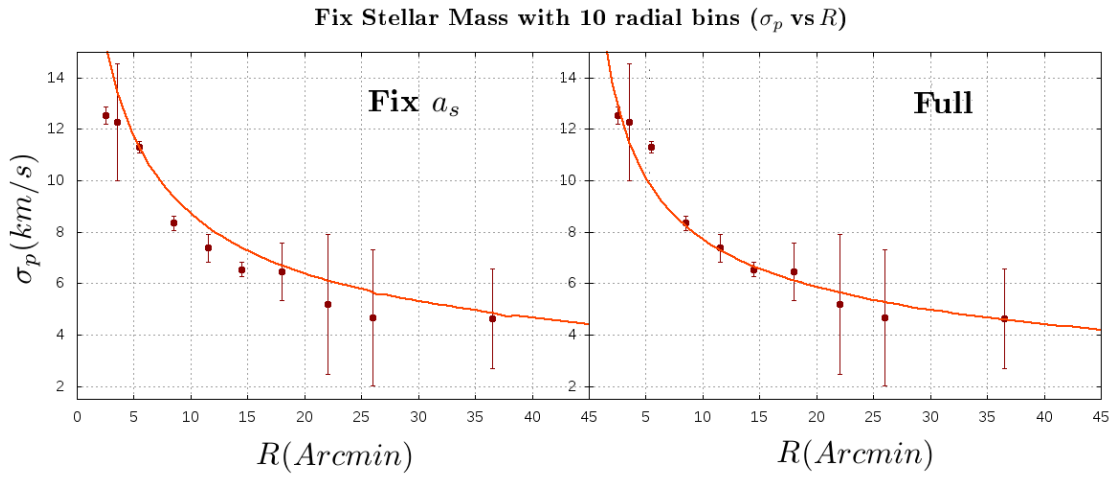
$$M_{sT} = 6.61 \times 10^6 M_\odot \quad (4.28)$$

This result is actually higher than some values of the dynamical mass found in the literature:

| Article | Mass (M_{\odot}) |
|--------------------------|----------------------|
| Mandushev et al. 1991 | 2.4×10^6 |
| Pryor & Meylan | 3.98×10^6 |
| Meylan et al. 1995 | 5.1×10^6 |
| Majewski et al. 2000 | 5.1×10^6 |
| Van de Ven et al. 2006 | 2.5×10^6 |
| Cassini et al. 2009 | 3.0×10^6 |
| Valcarce & Catelan, 2011 | 3.0×10^6 |
| Jalali et al. 2011 | 2.5×10^6 |

TABLE 4.5: Reported values of Omega Centauri's dynamical mass

The stellar mass should in principle, by smaller or at least equals to the dynamical mass, this discrepancy in our first approach to the mass determination is probably due to errors given by the extrapolation of the results of the detection area to the whole area of the cluster, because our detection area was very small ($\sim 0.2 \text{ arcmin}^2$) compared to the cluster's size of more than $6,000 \text{ arcmin}^2$. Still, the stellar population technique is consistent with the order of magnitude of the cluster's mass previously reported.

**FIGURE 4.10:** Tt.

| Experiment | β | $a_{\text{dm}}(\text{pc})$ | $a_s(\text{pc})$ | $M_{\text{dm}} (M_{\odot})$ | $M_s (M_{\odot})$ | Γ |
|------------|---------|----------------------------|------------------|-----------------------------|--------------------|----------|
| Fix a_s | 0.95 | 58.0 | 2.23 | 8×10^4 | 6.61×10^6 | 2.3 |
| Full | 0.96 | 7.36 | 50.0 | 1.35×10^6 | 6.61×10^6 | 1.88 |

TABLE 4.6: Ie

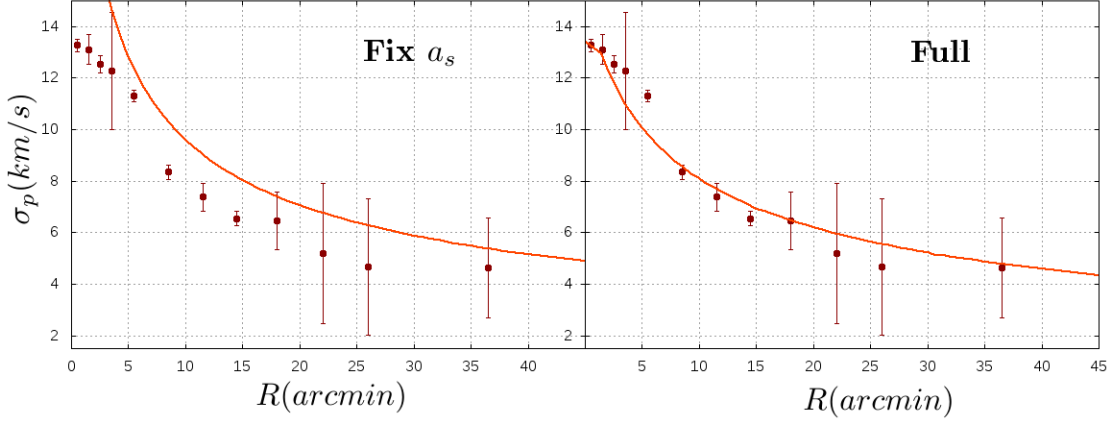
Fix Stellar Mass with 12 radial bins (σ_p vs R)

FIGURE 4.11: Tct.

| Experiment | β | $a_{dm}(pc)$ | $a_s(pc)$ | $M_{dm} (M_\odot)$ | $M_s (M_\odot)$ | Γ |
|------------|---------|--------------|-----------|--------------------|--------------------|----------|
| Fix a_s | 0.88 | 56.98 | 2.23 | 8×10^4 | 6.61×10^6 | 1.6 |
| Full | 0.96 | 7.6 | 12.0 | 6.88×10^5 | 6.61×10^6 | 0.9 |

TABLE 4.7: Ie

By taking an error bar of 25% we do the same procedures but with the smallest value of the mass that the error bar allows us to use, in this case the value of the stellar mass is $M_s = 4.9 \times 10^6 M_\odot$

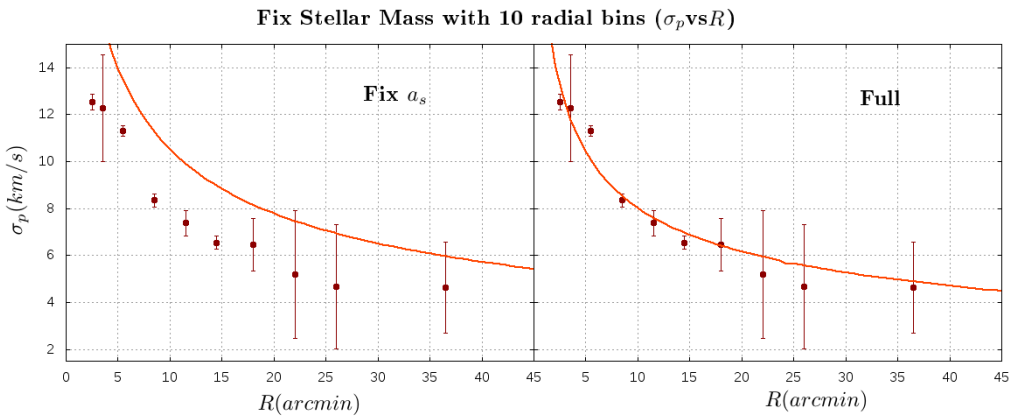
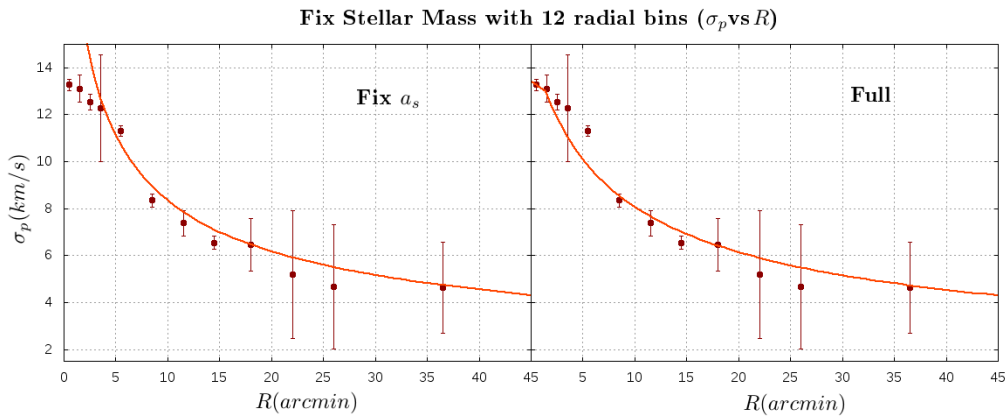


FIGURE 4.12: Tct.

| Experiment | β | $a_{\text{dm}}(pc)$ | $a_s(pc)$ | $M_{\text{dm}} (M_\odot)$ | $M_s (M_\odot)$ | Γ |
|------------|---------|---------------------|-----------|---------------------------|-------------------|----------|
| Fix a_s | 0.88 | 56.98 | 2.23 | 9×10^4 | 4.9×10^6 | 1.1 |
| Full | 0.92 | 7.26 | 37.98 | 1.35×10^6 | 4.9×10^6 | 0.72 |

TABLE 4.8: Ie**FIGURE 4.13:** Tct.

| Experiment | β | $a_{\text{dm}}(pc)$ | $a_s(pc)$ | $M_{\text{dm}} (M_\odot)$ | $M_s (M_\odot)$ | Γ |
|------------|---------|---------------------|-----------|---------------------------|-------------------|----------|
| Fix a_s | 0.88 | 56.98 | 2.23 | 9×10^4 | 4.9×10^6 | 0.82 |
| Full | 0.98 | 13.26 | 31.98 | 1.98×10^6 | 4.9×10^6 | 0.66 |

TABLE 4.9: Ie

Chapter 5

Conclusions

- Cfjsdkafdsjafkl

Bibliography

- [1] Michael J. Kurtz, Douglas J. Mink. *RVSAO 2.0: Digital Redshifts and Radial Velocities*. Harvard-Smithsonian Center for Astrophysics, Cambirdge, MA 02138, 1993.
- [2] Roueff F., Salati P., Tillet R. *The velocity dispersion profile of globular clusters: a closer look*. preprint astro-ph/9707174v1.
- [3] Binney J., Tremaine S.. *Galactic Dynamics*. Princeton University Press, 1994.
- [4] <http://news.ucsc.edu/2014/11/globular-clusters.html>
- [5] R. Ibata, C. Nipoti, A. Sollima et. al. *Do globular clusters possess Dark Matter halos?*. MNRAS, Ras 2012.
- [6] Joshua J. Adams, Karl Gebhardt, Guillermo A. Blanc et. al. *The central Dark Matter distribution of NGC 2976*. The Astrophysical Journal, 745:92 (17pp), 2012.
- [7] P. J. E. Peebles & R. H. Dicke. *Origin of the Globular Star Clusters*. The Astrophysical Journal, December 1968.
- [8] R. G. Gratton, E. Carreta, A. Bragaglia *Multiple populations in Globular Clusters*. The Astronomy and Astrophysics Review, 2012.
- [9] Richard B. Larson. *Globular Clusters as Fossils of Galaxy Formation*. Yale Astronomy Department.
- [10] M. E. Sharina, T. H. Puzia, V. L. Afanasiev et. al. *Globular clusters in low mass galaxies*. IAU Colloquium No. 198, 2005.
- [11] A. Klypin , A. V. Kravtsov et. al. *Where Are the Missing Galactic Satellites?* The American Astronomical Society, 1999.
- [12] M. Odenkirchen, E. K. Grebel, W. Dehnen et. al. *The extended tails of palomar 5: A 10° Arc of Globular Cluster Tidal Debris* The American Astronomical Society, 2003.

- [13] S. M. Fall & M. J. Rees. *A theory for the origin of Globular Clusters* The Astrophysical Journal, 298: 18-26, 1985.
- [14] C. Conroy, A. Loeb & D. Spergel *Evidence Against Dark Matter Halos Surrounding the Globular Clusters MGC1 and NGC 2419* The Astrophysical Journal, October 11th 2009.
- [15] S. S. Larse, J. P. Brodie et. al. *Nitrogen abundances and multiple stellar populations in the Globular Clusters of the Fornax DSPH* ApJ, accepted (27 Aug 2014).
- [16] V. Guglielmo, N. Amoruso, A. Colombo *Velocity dispersion in Elliptical Galaxies* The Sky as a laboratory, 2009.
- [17] Lars Hernquist *An analytical model for spherical galaxies and bulges* ApJ, 356:359-364, 1990 June 20.